

https://dspace.org/

Simulation of highly efcient solar cells

Aslan, Tahir

2018

https://hdl.handle.net/10539/26958

Downloaded from a DSpace repository. https://dspace.org/

UNIVERSITY OF THE WITWATERSRAND

DOCTORAL THESIS

Simulation of Highly Efficient Solar Cells

Author:
Tahir ASLAN

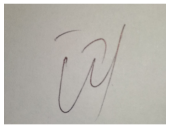
Supervisor:
Prof. Alexander QUANDT

A thesis submitted in fulfillment of the requirement of the degree of Doctor of Philosophy to the Faculty of Science, *University of the Witwatersrand, Johannesburg*

School of Physics

Declaration of Authorship

I hereby declare that this dissertation is my own work. It is being submitted for the Degree of Doctor of Philosophy of Science to the University of the Witwatersrand, Johannesburg. It has not been submitted before to any degree in any other University for assessment purposes.



Tahir ASLAN, October 1, 2018

UNIVERSITY OF THE WITWATERSRAND

Abstract

Faculty of Science
School of Physics

Doctor of Philosophy

Simulation of Highly Efficient Solar Cells

by Tahir ASLAN

In this thesis, we will consider problems causing losses in solar cells and try to solve these problems using numerical methods. We will simulate metal nanoparticles (MNPs) are embedded in order to enhance light absorption for thin film solar cells, which otherwise have insufficient absorption of light. To avoid thermal and sub-band losses, we will pick up the idea of using energy conversion processes in single junction solar cells, and discuss modeling of generic up-conversion (UC) and down-conversion (DC) processes, based on rare-earth ions in the context of solar cell device simulations. These numerical simulations are supposed to accompany future experimental studies and practical implementation of such processes in various types of inorganic solar cells. To understand and get parameters that we will need to determine extra current from frequency conversion, the Judd-Ofelt theory [1] has been used.

This work is organised as follows: After describing the basic working principles of a solar cell, we will give an introduction to modern solar cell device simulations, where we discuss the basic equations and simulation parameters [2] and show that most of the key parameters may be taken from ab initio numerical data, rather than experimental data. We will present various numerical approaches, photon absorption/emission processes and a more advanced approach using rate equations [3, 4]. Finally we discuss a simple strategy to implement UC and DC layers into solar cell device simulations. Note that this thesis is among the first systematic studies of implementing augmenting features into solid state device simulation, apart from crude estimates based on detailed balance models.

Acknowledgements

I would like to express my heartfelt gratitude to Professor Alexander Quandt, my supervisor, for giving me permission to undertake this research work and for his guidance on the progress of this work.

I would also like to acknowledge Dr. Robert Warmbier for his help to me with computational programs and numerical part of the project.

I would also like to acknowledge Prof. J. M. Keartland for their help on administrative issues.

I would like to thank Adam Shnier for going through my thesis and discussing the presentation of the science and writing, and for taking over space on my desk to keep his tea cup which he would use often while distracting me to have a good break when I needed it.

I would like to thank Itumeleng Mokgosi for always being willing to study together with me.

The work discussed in this thesis went smoothly due to the help of my work colleagues. I would like to thank Khalid Mohamed for helping me with *ab-initio* methods.

I would like to thank my wife, Felek Aslan, for her support throughout my time as a PhD student and for bearing with my absence when I attended to my studies.

The work discussed in this thesis would not have been possible without the financial support from the Materials for Energy Research Group (MERG).

Contents

Declaration of Authorship iii

Abstract v

Acknowledgements vii

1 Introduction 1
1.1 Motivation . . . 1
1.2 Objective . . . 2
1.3 Outline . . . 4

2 Fundamental of Solar Cells 5
2.1 Introduction . . . 5
2.1.1 Properties of Silicon . . . 5
Structure . . . 5
Band Gap . . . 6
P-N junction . . . 7
2.2 Current Density . . . 8
2.2.1 Dark current . . . 8
2.2.2 Photocurrent density . . . 9
2.3 J-V Simulation of Ideal c-Si Solar Cell . . . 11

3 Device Simulations of Solar Cell 13
3.1 Introduction . . . 13
3.2 Simulation Method . . . 14
3.2.1 J-V Curve . . . 16

4 Plasmonic Nanoparticles 19
4.1 Introduction . . . 19
4.2 Dielectric function . . . 19
4.2.1 Dielectric function Based on the Drude Model . . . 20
4.2.2 Dielectric Function Based on the Drude-Lorentz Model 21
4.3 Scattering and Absorption by Metal Nanoparticles . . . 23
4.3.1 Heat generated by plasmonic Nanoparticles . . . 30

5 Performance Enhancement of Solar Cells by Plasmonics Nanoparticles 35
5.1 Introduction . . . 35
5.2 Light Trapping by Metal Nanopatricles . . . 36
5.3 Silver and Gold Nanoparticles Embedded Randomly in Silicon 40

Optical Properties of Silicon 40
5.4 Optical properties of Composite Material 41
5.5 J-V Characterisation 44

6 Judd-Ofelt Theory **47**
6.1 Introduction 47
6.1.1 Glasses 47
6.1.2 Rare-Earth Ions 47
6.1.3 Spectroscopy of Rare-Earth Ions 48
Selection rules 49
6.2 Analysis of Jodd- Ofelt Theory 49

7 Up and Down Conversion and Their Application to Solar Cells **55**
7.1 Introduction 55
7.1.1 Photon absorption and emission theory 55
7.2 Up and Down Conversion 57
7.3 Rate Equations for Up/Down-Conversion 58
7.3.1 Up-Conversion Case 58
7.3.2 Down-Conversion Case 61
7.4 Simulation of an Ideal c-Si Solar Cell With and Without UP/-Down Conversion 63

8 Conclusions and Future Work **67**
8.1 Conclusions 67
8.2 Future Work 68

A Python Codes for Plotting **69**
A.1 Dielectric Function Based on the Drude-Lorentz Model 69
A.2 Scattering and Absorption by Metal Nanoparticles 70
A.3 Heat Generated by Metal Nanoparticles 72

B Publications And Conferences/Workshops Attended **75**
B.1 Publications 75
B.2 Conferences/workshops Attended 76

List of Figures

1.1 Typical losses by an inorganic solar cell. Photons which create thermalisation account for 35 per cent losses. Photons which have less energy than the band gap energy cannot generate the electricity and accounts for a 20 per cent loss (this figure was obtained from ref. [8]). 2

2.1 Diamond cubic lattice structure of silicon [25]. 6
2.2 Band structure of silicon [26]. 6
2.3 Scheme of absorption and transmission in a solar cell. When a solar cell is illuminated by photons, the electrons can use the energy of photons to jump from the valence band (VB) to the conduction band (CB), creating $electron - hole\ pairs$. Electrons with energies larger than the minimum of the conductive band (CB) lose their extra energy through thermalisation. The same happens for holes with energy lower than the maximum of VB. 7
2.4 Schema of a p/n-junction with space charge region. 8
2.5 J-V curve of an ideal c-Si solar cell in the dark, and under illumination. The short circuit current density J_{sc} is approximately equal to the photo current density J_p and open circuit voltage V_{oc} can be determined from the $J - V$ curve (see Fig. 2. 5). The arrow marks the current density J_m and the voltage V_m at the maximum power P_m. 12

3.1 Typical one-dimensional setting for solar cell device simulations. 13
3.2 Absorption coefficient of bulk Si, as computed using the Bethe-Salpeter equation and experimental result [34]. 16
3.3 Simulated $J - V$ characteristics for a silicon p/n-junction solar cell. 17

4.1 Experimentally imaginary and real part of the dielectric function ϵ for silver, and gold (experimentally data was obtained from ref. [43]). 20
4.2 Imaginary and Real part of the dielectric function for silver and gold by Drude model. 21
4.3 Imaginary and Real part of the dielectric function for silver and gold using the Drude-Lorentz model. This was plotted using the python code in the appendix A.1. 22
4.4 Shifted scattering and absorption cross-section of Ag Np by different media. ($r = 30\ nm$) 24

4.5 Scattering and absorption cross-section for Au and Ag Nps as a function of the wavelength, and for various radii of the metallic Nps. The dielectric function of the surroundings is $\epsilon_m = 1.8$ which is corresponding to ice. This was plotted using the python code in the appendix A.2. 25
4.6 SEM images of ellipsoidal Ag Nps. The figure was obtained from ref. [52]. 26
4.7 Schema of prolate and oblate ellipsoid. 27
4.8 Absorption cross-section of Ag and Au prolate and oblate ellipsoids. (A) In the prolate case; a, b and c are 24 nm, 12 nm and 12 nm, respectively and in the oblate case; a, b and c are 24 nm, 24 nm and 12 nm, respectively and (B) in prolate case; a, b and c are 48 nm, 24 nm and 24 nm, and in oblate case; a, b and c are 48 nm, 48 nm and 24 nm, respectively. $\epsilon_m = 2.25$. 28
4.9 Scattering cross-section of Ag and Au prolate and oblate ellipsoids. (A) In the prolate case; a, b and c are 24 nm, 12 nm and 12 nm, respectively and in the oblate case; a, b and c are 24 nm, 24 nm and 12 nm, respectively and (B) in prolate case; a, b and c are 48 nm, 24 nm and 24 nm, and in oblate case; a, b and c are 48 nm, 48 nm and 24 nm, respectively. $\epsilon_m = 2.25$. 29
4.10 Temperature changes for different flux intensities as a function of the wavelength in an environment with $\epsilon_m = 1.8$. The radius r, of the Np is 20 nm. 31
4.11 (a) Temperature change as a function of distance and (b) temperature change for an array of 3x4 Nps as a function of x, y coordinates ($R_{Np} = 20\ nm$). The initial flux intensity is $I_0 = 1 \times 10^8\ W/m^2$. This was plotted using the python code in the appendix A.3. 32
4.12 Temperature gradient of one and 12 Nps as a 3x4 array as a function of wavelength at $R_{Np} = 70\ nm$ and $R_{Np} = 20\ nm$. The distance between Nps is 100 nm and the initial flux intensity is $I_0 = 1 \times 10^8\ W/m^2$. 33

5.1 Configuration of random Au Nps in the solar cell (this figure was obtained from ref [57]). 35
5.2 Extinction cross-section of Au and Ag as a function of radius. 37
5.3 (a) Real and imaginary part of effective dielectric function of $Si - Ag$ composite material and (b) Real and imaginary part of effective dielectric function of Si-Au composite material ($R_{np} = 10\ nm$ and $f_s = 0.05$). 39
5.4 Absorption coefficient of bulk silicon. 40
5.5 Imaginary and real part of dielectric function and refractive index of bare Si [60]. 41
5.6 Absorption coefficient of bare bulk silicon, silicon with Ag Nps, and silicon with Au Nps. 42

5.7 Absorbance of composite material (a) silicon with spherical gold Nps and (b) silicon with spherical silver Nps (here f_s = 0.05, R_{np} = 10 nm and $L = 1\ \mu m$). 43
5.8 Absorption coefficient of bare bulk silicon, silicon with Ag Nps and silicon with Au Np (used Eq. 5. 7). 44
5.9 J-V curve for thin-film c-Si solar cell simulated using GPVDM. 45

6.1 Energy levels of rare-earth ions in the $4f^n$ configuration. Adopted from ref. [76] 50
6.2 Energy level diagram for Dy^{+3} in a glass with possible transitions. Adopted from ref. [82] 52
6.3 Emission cross-section of $Dy : CaBA$. where the excitation wavelength is $\lambda = 355\ nm$. 53
6.4 Energy-level scheme of the Nd^{+3}-doped 54

7.1 Absorption and emission process between two energy levels. . 56
7.2 Schematic view of a solar cell with UC and DC layers. 58
7.3 UC energy level diagram with the most important processes for Tm^{3+} in the fluoride glass [90]. 59
7.4 Population density of state N_1, N_3 and N_5 as a function of pump power for the UC system of Eq. 7. 10. 61
7.5 DC energy level diagram with the important processes for Tb^{3+}-Yb^{3+}. 62
7.6 J-V for ideal c-Si solar cell, and with UC/DC materials. 65

List of Tables

2.1 Parameters for the model of a reference current density in Si . 11
2.2 Performance of c-Si solar cell. 12

3.1 The main input parameters for a thin film Si p/n junction solar cell. 16
3.2 Performance of thin film Si solar cell. 17

4.1 The parameters for a Drude-Lorentz model of Au and Ag . . . 22

5.1 The main input parameters for a thin film c-Si p/n junction solar cell. 45
5.2 Performance of a thin film c-Si solar cell with and without embedded plasmonic Nps. 46

6.1 Selection rules for various types of transition in rear-earth ions [74]. 49
6.2 Necessary parameters for plotting absorption cross-section of $Dy : CaBA$ [84]. 54

7.1 Parameters for solving the rate equations of Eq. 7. 10. 60
7.2 Parameters for solving the rate equations of DC [92]. 63
7.3 Performance of the c-Si solar cell with the UP/DC conversion layer. 64

List of Abbreviations

UC	**U**p **C**onversion
DC	**D**own **C**onversion
UV	**U**ltraviolet
IR	**I**nfrared
QE	**Q**uantum **E**fficiency
VB	**V**alance **B**and
CB	**C**onduction **B**and
DFT	**D**ensity **F**unctional **T**heory
BSE	**B**ethe **S**alpeter **E**quation
Np	**N**anoparticle
RE	**R**are **E**earth
JO	**J**udd **O**felt
GSA	**G**round **S**tate **A**absorption
EST	**E**xited **S**tate **A**absorption
SPA	**S**pontaneous **E**mission
ET	**E**nergy **T**ransfer

For Humanity...

Chapter 1

Introduction

1.1 Motivation

Solar cells are devices that convert solar photon energy directly into electric energy. Solar energy plays a major role among renewable energy sources, first of all it is sustainable and it is environmentally friendly. Among the so-called sustainable energy sources are solar energy, wind power and hydro power [5].

The price of commercial inorganic solar cells has become much cheaper than electricity from coal or nuclear power plants. Furthermore, most energy sources such as, fossil fuels and nuclear have risks which are social, economic, and environmental [6]. For such an important energy technology like solar energy it is important to keep improving performance and reducing costs. This can accelerate the adoption and broaden the use of photovoltaics.

In order to reduce costs and reduce the amount of material used in a solar cell, researchers have used thin film solar cells. The thin film solar cells include second generation solar cells (thicknesses $1 - 2$ μm), such as solar cells based on cadmium telluride, copper indium diselenide, amorphous and polycrystalline silicon. Typically these thin film solar cells are more efficient light absorbers, yet because of how thin they are, they do not absorb all of the incident photons. Furthermore not all of the incident photos can be used, and not all of the photons that can be used are actually used very efficiently.

To see how we can improve how single junction solar cells use light we look at the solar spectrum starting with Ultra Violet (UV) and later discussing lower energy photons that are mostly in the infra-red region. Light that comes from the sun spans the UV across the infrared spectral range, but a solar cell such as Si can use photons only from the visible region and the rest is not utilised. The main losses in typical semi-conductor solar cells are due to the thermalisation of electrons in the UV and the visible range of the solar spectrum, the inability to absorb photons with energies below the electronic band gap, and losses due to the recombination of electrons and holes, in particular at the contacts. An ideal solar cell at room temperature may be described as a combination between acting like a black-body absorber and a carnot engine [7]

Note that photons which have less energy then the band gap energy are not able to create *electron − hole pairs* and the corresponding photocurrent, and the photons which have a higher energy than the band gap increase the temperature of the cell. As shown in Fig. 1. 1 out of a 55 per cent loss in energy, 20 per cent is lost due to photons with a sub-band-gap energy (mostly in the infra-red region) and, 35 per cent due to photons with energy above the band gap (for silicon that has a 1.2 eV band gap energy which means that only the photons in visible range may be harnessed with minimal losses). The photons which are useful for generating electricity are the ones that have the energy close to the band gap of the solar cell. Therefore, the ideal single junction solar cell with a single band gap and no resistance losses at the contacts can be at most 35 per cent efficient. But it is not able to use the full photon spectrum [6].

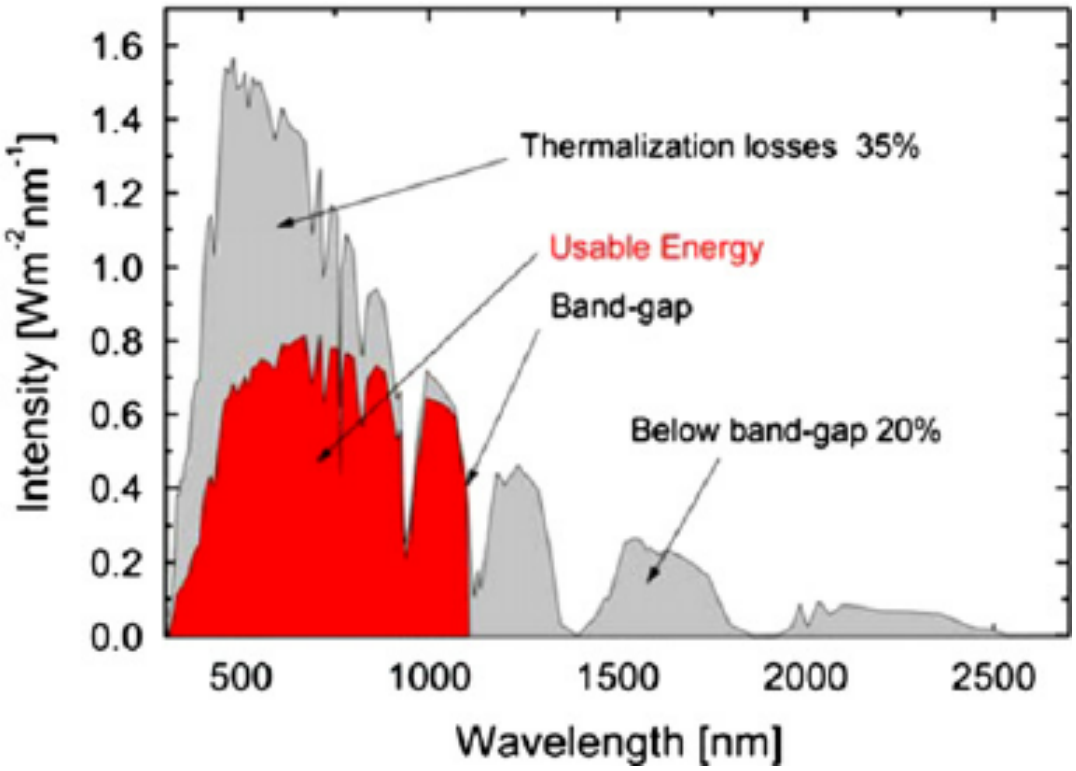


FIGURE 1.1: Typical losses by an inorganic solar cell. Photons which create thermalisation account for 35 per cent losses. Photons which have less energy than the band gap energy cannot generate the electricity and accounts for a 20 per cent loss (this figure was obtained from ref. [8]).

1

1.2 Objective

The aim of this study is to understand fundamental losses of solar cells and use numerical methods to suggest how to improve their efficiency towards the

theoretical limits. The efficiencies of silicon based solar cells are getting closer and closer to the theoretical limit of 34 per cent for single-junction silicon based solar cells, as estimated by Shockley and Queisser in 1961 [9]. These impressive numbers must however be compared to the theoretical efficiency limit of 85 per cent for a generic photovoltaic device [10], which shows that there is plenty of room for improvements.

Frequency conversion processes are not part of standard device simulations, these must be introduced through additional functional layers containing rare-earth ions. After absorption of an incoming photon, the emission of up- or down-converted photons leads to additional photon flux in a frequency range, where the solar cell has much better conversion efficiencies. Thus, the implementation of generic frequency conversion processes in solar cell simulations boils down to the calculation of the additional photon fluxes that result from the frequency conversion processes in these additional functional layers. A promising strategy for single junction solar cells is to convert UV and IR into a frequency range with minimum thermal losses close to the generic electronic band gap (as suggested by Trupke [11]).

The suggested methods are upcoversion (UC) [12] and downconversion (DC) [13]. UC converts lower frequency photons into higher frequency photons. Hence, it converts photons that have sub-band-gap energy, into photons with energies above the band gap. DC converts higher energy photons into less energetic photons which also reduces thermalisation losses (see Fig. 1. 1). This work will investigate UC and DC techniques applied to inorganic solar cells. To get a rough idea about enhancing the efficiency of solar cells let us have a look at the photocurrent, J_p, over photon energy, E, is

$$J_p = qQE \int_{E_1}^{E_2} \Phi_{1.5G}(E) dE \tag{1.1}$$

Where QE is the quantum efficiency and $\Phi_{1.5G}(E)$ is the solar photon flux on earth. Here, we assume that all photons generate an $electron - hole$ pair. By using this equation we can calculate additional current densities from UC and DC. In the case of UC, the QE is 50 per cent and we integrate the solar spectrum from half of the energy of the band gap which is equivalent to $E_1 = 0.6\ eV$ to the energy of the full band gap (for Si $E_g = 1.1\ eV$). The additional photocurrent from the UC is equal to 86 $\frac{A}{m^2}$. In the case of DC, QE is 100 per cent, the additional current is equal to 116 $\frac{A}{m^2}$ (integration between $E_1 = 4.4 - E_1 = 2.2\ eV$). We will discuss more comprehensive UC and DC efficiency calculations later on by modeling a conventional Si solar cell and with a layer containing rare earth ions (Tm or Tb and Yb) for the frequency conversion processes.

The other aim is to increase the absorption of light into thin film solar cell [14–16], for example embedding metal plasmonic nanoparticles in the cell.

The plasmonic nano-particles will increase the absorption of light, and preferentially scatter photons into the layer of solar cells. We will study this phenomena in considerable detail. It is also known that the nanoparticles will generate heat affecting their surroundings and we will develop a suite of simulations to predict this phenomena, including the cord field effect.

Finally we will also simulate solar cell devices for the development of more efficient types of solar cells. The key parameters will be taken from *ab initio* numerical data.

1.3 Outline

This thesis discusses numerical simulations to improve the efficiency of solar cells. Chapter 2 presents the fundamentals of solar cells. Chapter 3 presents simulation methods of solar cells. Chapter 4 presents optical properties of nanoparticles. Chapter 5 presents methods of simulation and other techniques that are used for the enhancement of the efficiency of solar cells. Chapter 6 presents the Judd-Ofelt theory and calculates analytically some important parameters such as the life time of photon emissions and furthermore, it gives brief information about the spectroscopy of rare-earth ions. Chapter 7 presents a brief discussion of up-conversion and down-conversion, applied to a c-Si solar cell and calculates how much the efficiency can theoretically be enhanced.

In general, this study should stimulate further experimental and theoretical (numerical) experiments into the use of frequency conversion and plasmonics techniques, with the goal to enhance the efficiency of conventional solar cells.

Chapter 2

Fundamental of Solar Cells

2.1 Introduction

We will give a brief history of solar cells as a background to the technology. In 1839, the photovoltaic effect was first described by Edmund Bequerel. After 25 years Willoughby Smith described the Effect of Light on Selenium [17]. The first solid state photovoltaic cell was built by Charles Fritts in 1883 but it was only around 1 per cent efficient. After Albert Einstein explained the photoelectric effect in 1905 and Vadim Lashkaryov discovered the p-n-junction in 1941 [18, 19], Calvin Souther Fuller, Daryl Chapin and Gerald Pearson invented the first practical photovoltaic cell in 1954. [20, 21]. The scientific community focused only on silicon solar cells until 1990. In the early 1990s multijunction photovoltaic cells used on spacecraft including gallium-arsenide [22].

As mentioned in the previous chapter, a solar cell is a device that converts photon energy into electric energy. The most common commercial type of solar cell is the Si based solar cell. In the following chapter we will develop a reference model for an ideal crystalline silicon (c-Si) solar cell. But before we go through the technical details, we will discuss the fundamental properties of the Si semiconductor which play a significant role in a solar cell such as the structure and the band gap of Si. Finally we explain the physics of a typical p/n-junction [23, 24].

2.1.1 Properties of Silicon

Structure

Silicon (Si) is a group IV element and its crystal structure is a cubic diamond lattice (Fig. 2. 1). Si has the atomic number 14, its atomic weight is 28.085, and the electron orbital configuration is $1s^2 2s^2 2p^6 [3s^2 3p^2]$.

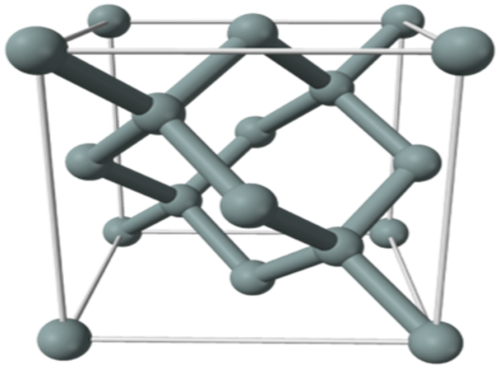


FIGURE 2.1: Diamond cubic lattice structure of silicon [25].

Band Gap

Silicon is a semiconductor and it has an indirect band gap, as we can see from Fig 2. 2 [26]. Silicon can conduct heat reasonably well which becomes important to remove thermal energy, which was produced by the thermalisation of charge carriers.

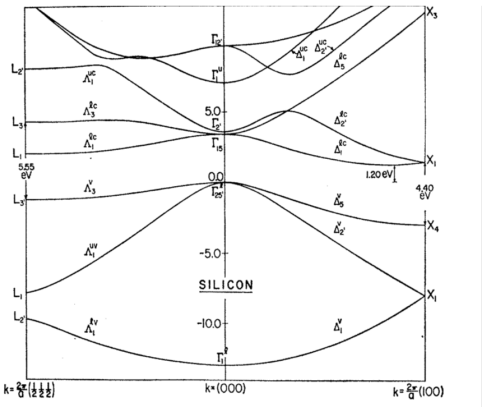


FIGURE 2.2: Band structure of silicon [26].

The band gap of silicon directly affects the efficiency of Si based solar cells. Silicon has a band gap of $E_g \sim 1.1\ eV$ and the energy photons coming from the Sun are across a range between ≈ 0.4 to $\approx 6\ eV$. Fig. 2. 3 demonstrates very well that the photons absorbed have a higher energy than the band gap energy, increase temperature. As the temperature of a solar cell increases due to thermalization of energetic photons the efficiency of the solar cell decreases, and the photons that have less energy than the band gap (sub-band gap energy photons) are transmitted through the solar cell without being utilised. Therefore, the ideal case for solar cells is that all photons will have an energy close to the band gap energy.

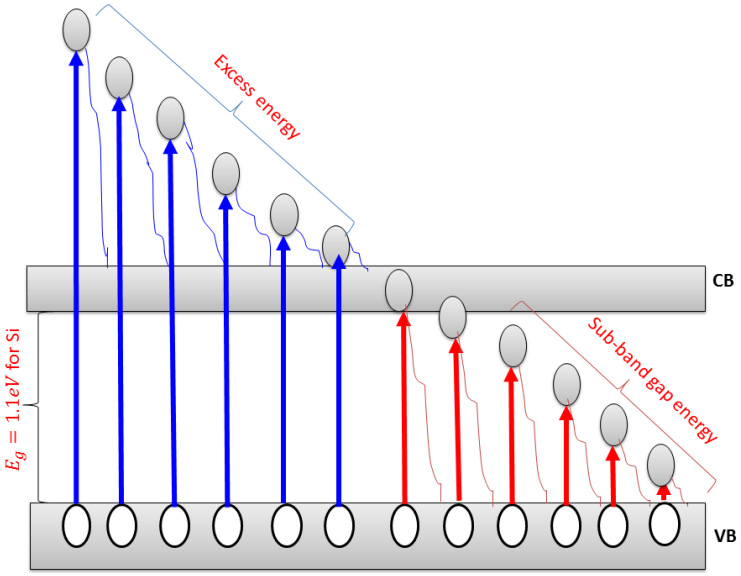


FIGURE 2.3: Scheme of absorption and transmission in a solar cell. When a solar cell is illuminated by photons, the electrons can use the energy of photons to jump from the valence band (VB) to the conduction band (CB), creating *electron − hole pairs*. Electrons with energies larger than the minimum of the conductive band (CB) lose their extra energy through thermalisation. The same happens for holes with energy lower than the maximum of VB.

P-N junction

A p-n junction is formed by contact between p and n-type semiconductors. The p-type has mostly positively charged carriers and the n-type has mostly negatively charged carriers which are induced by dopants that have fewer valence electrons than Si (p-dopants) or more valance electrons than (n-dopants). In practice the doping of silicon with boron (B) results in a p-type and phosphorus (P) an n-type. When the p-type and n-type are separated or isolated from each other it is a reasonable assumption that, the charge carriers are distributed homogeneously and that the density of the electrons n is equal to the density of ionized donors N_D, and density of the holes p is equal to the density of the ionized acceptors N_A,

$$n = N_D, p = N_A$$

At thermal equilibrium

$$np = n_i^2 \tag{2.1}$$

Where n_i is the so-called intrinsic carrier density. When the p and n types are brought together as in solar cells, the original thermal equilibrium of the free charge carriers in the materials is destroyed through the diffusion of the majority charge across the interface and a new equilibrium is reached,

resulting in an electric field E at the junction, called the space charge region. This is shown in Fig. 2. 4.

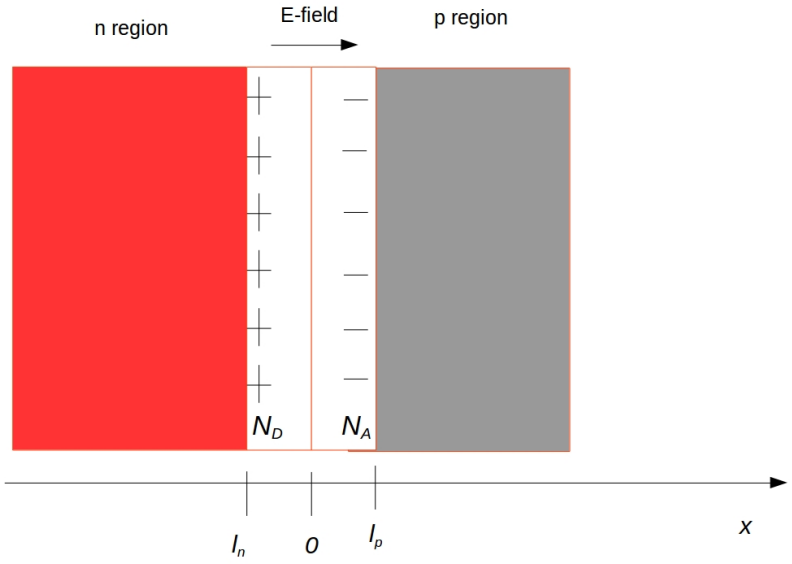


FIGURE 2.4: Schema of a p/n-junction with space charge region.

2.2 Current Density

In the following we discuss the various methods that describe current flow in a typical inorganic solar cell under an applied electric field. We will introduce important concepts like the dark current J_{dark}, the photo current J_p and the efficiency of a solar cells.

2.2.1 Dark current

From an electronic point of view p/n-junction acts as a diode. At low voltages it lets an electronic current flow primarily in one direction since it has lower resistance in one direction and higher resistance in the other. This leads to a rectification of currents flowing through the device. The size of the space charge region is affected by the magnitude and direction of the electric field. [27]. If an external voltage, V, is applied to a p/n junction in the dark, a dark current density J_{dark} will be generated, which is given by the diode equation [23, 28]

$$J_{dark} = J_0(e^{\frac{qV}{k_B T}} - 1) \tag{2.2}$$

where T is temperature, k_B is Boltzmann's constant, q is electron charge and J_0 is the saturation current density at V=0 (constant). The latter is given by:

$$J_0 = J_{diff} + J_{scr} + J_{rad} \tag{2.3}$$

where J_{diff} is the diffusion current density, which is:

$$J_{diff} = qn_i^2\left(\frac{D_n}{N_A l_n} + \frac{D_p}{N_D l_p}\right) \tag{2.4}$$

where l_n and l_p are diffusion lengths for n and p regions, D_n and D_p are diffusion coefficients for the n and p region, N_A is the acceptor doped density, N_D is the donor doped density and J_{src} is the recombination current density

$$J_{src} = qn_i\frac{w_n + w_p}{\sqrt{\tau_n \tau_p}} \tag{2.5}$$

where w_n and w_p the size of the depletion region on the $n-$ and $p-$side and τ_n and τ_p are the lifetimes of electrons and holes in n and p region. J_{rad} is the radiative recombination current density which takes into account the current density contribution from the direct band gap material [23]. Also note the temperature dependence in Eq. 2. 2.

2.2.2 Photocurrent density

The solar cell absorbs photons under illumination which leads to the creation of *electron-hole* pairs in the space charge region. These *electron-hole* pairs are separated to be used in an external circuit. Now we describe a p/n- junction under illumination which drives the system out of equilibrium resulting in a photocurrent J_p.

In order to calculate the percentage of photons absorbed by the solar sell we first need to know the reflectivity of and the absorption coefficient of the solar cell. The relation between the reflective index $\tilde{n}(\lambda)$ and the dielectric function $\tilde{\epsilon}(\lambda)$ as a function of the photons wavelength λ of a material is given by [29]

$$\tilde{n}(\lambda) = \sqrt{\tilde{\epsilon}(\lambda)} \tag{2.6}$$

$\tilde{n}(\lambda)$ has a real and a imaginary part which is related to the real part and the imaginary part of $\tilde{\epsilon}(\lambda)$ and can be described by:

$$\tilde{n}(\lambda) = n(\lambda) + i\kappa(\lambda) \tag{2.7}$$

where the real component $n(\lambda)$ is the refractive index and the imaginary component $\kappa(\lambda)$ is the extinction coefficient, which is proportional to the absorption coefficient $\sigma(\lambda)$ [24] by:

$$\sigma(\lambda) = 4\pi\frac{\kappa(\lambda)}{\lambda} \tag{2.8}$$

The reflectivity can be calculated from either the dielectric function $\tilde{\epsilon}(\lambda)$ or the absorption coefficient $\sigma(\lambda)$ as shown in the following text. The fraction of the photons that are absorbed by the solar cell is described by the reflectivity $R(\lambda)$ of a material. The reflectivity is the fraction of the incident photons that are reflected from the solar cell:

$$R(\lambda) = \left| \frac{\tilde{n}_0 - \tilde{n}_1}{\tilde{n}_0 + \tilde{n}_1} \right|^2 \tag{2.9}$$

where $\tilde{n}_0 = 1 + i0$ is the refractive index of air and $\tilde{n}_1$ is the complex reflection index of the semiconductor. The transmitted T which is the fraction of the photons that are absorbed by the material is:

$$T = 1 - R \tag{2.10}$$

Next we describe the solar photon flux density $\Phi(E)$. As we can see from Fig. 1. 1 the sun emits the photons which have an energy including a range from ultraviolet to infrared, and most of the incoming energy is concentrated in the visible range ($300 - 800\ nm$). We can convert the wavelength λ to the energy E of the photon which is given by

$$E = hc/\lambda \tag{2.11}$$

where h is Planck's constant and c is the speed of light. The solar photon flux density $\Phi(E)$, is given by [23]

$$\Phi(E) = \int \frac{2F_s}{h^3c^2} \left(\frac{E^2}{e^{\frac{E}{k_B T}} - 1} \right) dE \tag{2.12}$$

where F_s is a geometric factor, which is dependent on the angle between the Sun and surface normal, E is the energy of photons, c is the speed of light. In this case the solar spectrum will be the one on the surface of the earth using the AM 1. 5 (air-mass 1. 5) model, which is the literature standard [30]. The photocurrent is given by [23]

$$J_p = q \int_{E_1}^{E_2} \eta(E) T a(E) \left(\frac{2F_s}{h^3c^2} \left(\frac{E^2}{e^{\frac{E}{k_B T}} - 1} \right) \right) dE \tag{2.13}$$

where $\eta(E)$ is the probability for the charge carriers to be collected, $a(E)$ is the probability of the absorption of a photon. k_B, T and h were defined previously. For the so-called gate maximum, all photons that have energy higher than the band gap energy ($E > E_g$) are absorbed and each photon in this range generates one $electron - hole\ pair$. Which means $\eta = 1$ and $a = 1$. It was assumed that the series and shunt resistance were zero. The basic $J - V$ characteristic of a p-n junction/solar cell may be described by a modified

diode equation including the photocurrent [10]

$$J_{net} = J_o \left(e^{\frac{eV}{\kappa_B T}} \right) - J_p \tag{2.14}$$

Again J_o is a saturation current for $V \rightarrow -\infty$, and J_p is related to the current generated by the incoming light. Next we will look at a conventional type of Si based solar cell, calculate a model $J - V$ curve and determine the corresponding efficiency.

2.3 J-V Simulation of Ideal c-Si Solar Cell

A ideal c-Si solar cell was simulated using Eqs 2. 2, 2. 13 and 2. 14 and the data given in Table 2. 1. Here the dark current density J_{dark} and photocurrent density, J_p parameters are given by table 2. 1. Fig. 2. 5 shows the J_{dark} as a function of the applied voltage and the net current J_{net} including the photocurrent, and where we were marking the so-called maximum power point.

Parameters	Symbol	Value
Intrinsic carrier concentration $[m^{-3}]$	n_i	15×10^{16}
Acceptor doped $[m^{-3}]$	N_A	10^{23}
Donor doped $[m^{-3}]$	N_D	10^{25}
The minor carry diffusion length for n and p region $[m]$	l_n and l_d	500×10^{-6} and 10×10^{-6}
Diffusion coefficient for n and p region $[m^2 s^{-3}]$	D_n and D_p	2.58×10^{-3} and $2.58 \times 1.^{-4}$
Charged region of n and p side $[m]$	$\omega_n + \omega_p$	1×10^{-7}
Boltzmann's constant $[m^2 kg s^{-2} K^{-1}]$	κ_B	1.38×10^{-23}
Temperature $[K]$	T	300

TABLE 2.1: Parameters for the model of a reference current density in Si

The photocurrent shown was determined using Eq 2. 13 and was integrated from $E_1 = 1.1\ eV$ to $E_1 = 4.1\ eV$, see Fig. 2. 5.

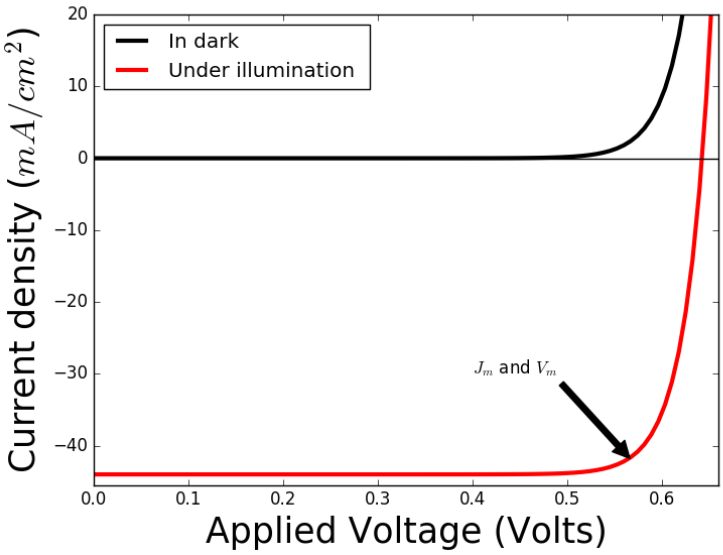


FIGURE 2.5: J-V curve of an ideal c-Si solar cell in the dark, and under illumination. The short circuit current density J_{sc} is approximately equal to the photo current density J_p and open circuit voltage V_{oc} can be determined from the $J-V$ curve (see Fig. 2. 5). The arrow marks the current density J_m and the voltage V_m at the maximum power P_m.

Note that at the maximum working point, J_M and V_M can be obtained from:

$$\frac{dP}{dV}\Big|_{V_m} = 0 \text{ (maximum power)}, \tag{2.15}$$

Thus using the fact that $P = J \cdot V$ and using Eq. 2. 14 we obtain

$$\begin{aligned} V_M &= \frac{\kappa_B T}{q} ln\Big(\frac{1 + J_p/J_0}{1 + qV_M/\kappa_B T}\Big) \\ J_M &= J_0(e^{qV_m/\kappa_B T} - 1) - J_p \end{aligned} \tag{2.16}$$

The power conversion efficiency of the solar cell is the most important figure of merit to gauge the performance of a solar cell. It is defined by

$$\eta = \frac{P_{out}}{P_{in}} \times 100\% \tag{2.17}$$

where $P_{out} = J_m \times V_m$ is the output power density and $P_{in} = 1000\ W/m^2$ is input solar power density. From Fig. 2. 5 we get:

J_{sc}	V_{oc}	J_m	V_m	η
440 A/m^2	0.67 V	$\approx$ 420 A/m^2	$\approx$ 0.57 V	$\approx$ 24%

TABLE 2.2: Performance of c-Si solar cell.

Chapter 3

Device Simulations of Solar Cell

3.1 Introduction

Device simulations are a crucial part of the development of novel and more efficient types of solar cells because they allow us to test an idea or device before the potentially costly and time consuming experimental studies. The necessary simulation parameters are usually taken from experiment. But it turns out that most simulation parameters can be taken from *ab-initio* data and sometimes experimental data is not needed. In this work we will use data from both experimental and *ab-initio* sources.

In general the simulation of solar cell devices is mostly considered a one-dimensional problem, where the physical properties are functions of the z-direction perpendicular to the various layers of the device. This is illustrated in Fig. 3. 1, where light falls on a layered photovoltaic device, which is basically a classical p-n junction with back and front contacts.

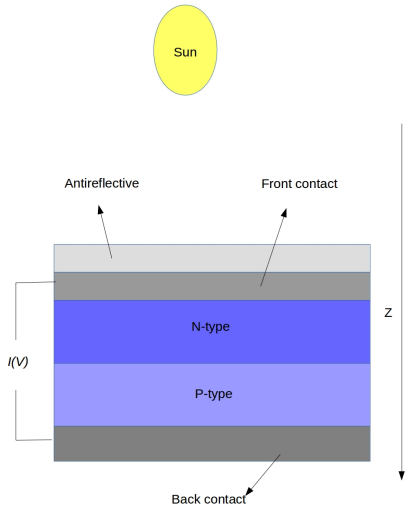


FIGURE 3.1: Typical one-dimensional setting for solar cell device simulations.

The device is covered by an anti-reflective coating on the side exposed to sunlight. Photons may enter the device from this side, and they get absorbed by the active layers of the solar cell. When this happens free charge carriers (electrons and holes) are created. These free charge carriers give rise to the current density J and the voltage V generated by the solar cell. First we discuss the simulation method then the characterisation of the performance of our simulated solar cell.

3.2 Simulation Method

Modern device simulation codes for solar cells predict similar $J-V$ characteristics (and other related physical properties) [2]. To get an idea about the distribution of the electric fields within a p/n- junction, we have to analyse Poisson's equation [31]. Poisson equation is

$$\frac{d}{dz}\left(-\epsilon(z)\frac{d\varphi}{dz}\right) = e[p(z) - n(z) + N_D(z) - N_A(z)] \tag{3.1}$$

Where $n(z)$ and $p(z)$ are free carrier densities for electrons and holes respectively, ϵ is the dielectric constant, $\varphi(z)$ is the electric potential which gives rise to the overall cell potential V and $N_D(z)$ and $N_A(z)$ are donor and acceptor densities [32]. The Poisson's equation can be solved by the iteration method under suitable boundary conditions [31]. The dielectric constant $\epsilon(z)$ of the basic materials can either be taken from experiment, or calculated from first principles [33], as we will discuss below. In order to determine the corresponding change in electron and hole current density $J_n(z)$, $J_p(z)$, we need to solve two related continuity equations:

$$\begin{aligned} \frac{1}{e}\frac{d}{dz}\left(J_n(z)\right) &= -G_{opt}(z) + R(z); \\ \frac{1}{e}\frac{d}{dz}\left(J_n(z)\right) &= -G_{opt}(z) + R(z) \end{aligned} \tag{3.2}$$

Here $G_{opt}(z)$, $R(z)$ are the (optical) generation and recombination rates. Note that the generation rates $G_{opt}(z)$ can be calculated from first principles, given the known photon flux $\Phi(\omega, z)$. This will also be used below. The currents themselves are given by the following expressions:

$$\begin{aligned} J_n(z) &= e\mu_n n(z)E(z) + qD_n\frac{dn(z)}{dx}; \\ J_p(z) &= e\mu_p p(z)E(z) - qD_p\frac{dn(z)}{dx} \end{aligned} \tag{3.3}$$

where μ_n, μ_p are electron and hole mobilities, which can be taken from first principles calculations [34], D_n and D_p are the diffusion coefficients of electrons and holes respectively and $E(z)$ is electric field. This completes the set of equations to be solved for each point on a path in z-direction, after imposing the proper boundary condition between the different layers [2].

The recombination rates $R(z)$ are [2]

$$\begin{aligned} R(z)_n &= \frac{\triangle n(z)}{\tau_n} \\ R(z)_p &= \frac{\triangle p(z)}{\tau_p} \end{aligned} \tag{3.4}$$

Where $\triangle n(z)$ and $\triangle p(z)$ are the excess electron and hole concentration and τ_n and τ_p are the lifetime of electrons and holes respectively. The rate at which free charge carries are generated as a function of the energy of photons E, is described by

$$G_{opt}(E) = \alpha(E)\phi_n(E) \tag{3.5}$$

Where $\alpha(E)$ is the absorption coefficient and $\phi(E,z)$ is the solar photon flux (or any other external source of photons). After the substitution of Eq. 3. 4 and 3. 3 into Eq. 3. 2, we get the following second-order differential equations below:

$$\begin{aligned} D_n \frac{d^2\triangle n(z)}{d^2x} - \frac{\triangle n(z)}{\tau_n} + G(z) = 0 \\ D_p \frac{d^2\triangle p(z)}{d^2x} - \frac{\triangle p(z)}{\tau_p} + G(z) = 0 \end{aligned} \tag{3.6}$$

Here the equation can be solved under the appropriate boundary condition to get J_n and J_p [35]. Finally, the total photo-current density is

$$J_{ph} = J_n + J_p + J_{dep} \tag{3.7}$$

where J_{dep} is current density coming from depletion layer (see ref. [31]) The current density is

$$J = J_{dark} - J_{ph} \tag{3.8}$$

as described in the previous Chapter.

The absorption coefficient $\alpha(E)$ can be determined from first principles [33], using Density Functional Theory (DFT). With DFT one can also reliably compute all the ground-state properties, which may be derived from the electronic ground state density. But optical properties like $\alpha(E)$ are not based on the ground state. Therefore one needs methods that go beyond DFT, where the optical properties of a material can be calculated either by using the Linear Response Time-Dependent DFT, or based on the Bethe-Salpeter equation (BSE) [36, 37]. Of these two basic approaches, the BSE is the more accurate method, but it is also more cumbersome from a numerical point of view.

An example of such a calculation is shown in Fig. 3. 2. Here we depict the numerical absorption coefficient for bulk Si and a corresponding experimental result which are very close to each other. The accuracy of BSE approach is primarily limited by the computational resources available. Fortunately,

device simulations are not very sensitive to the fine details of the absorption spectrum, which makes them an ideal application for *ab- initio* computations.

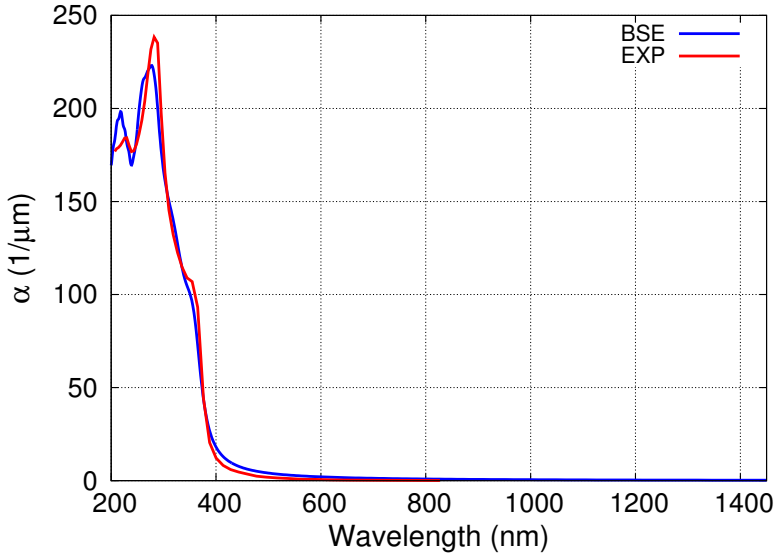


FIGURE 3.2: Absorption coefficient of bulk Si, as computed using the Bethe-Salpeter equation and experimental result [34].

3.2.1 J-V Curve

We now carry out a typical device simulation, using the GPVDM program package [38]. The main input parameters required for such a device simulation are the electric materials and optical properties for each respective layer of the solar cell device (see table 3. 1).

Parameters	Symbol	Value
Electron mobility $[\frac{cm^2}{Vs}]$	μ_n	1350
Hole mobility $[\frac{cm^2}{Vs}]$	μ_p	480
Donor doping concentration $[m^{-3}]$	N_D	10^{22}
Acceptors doping concentration $[m^{-3}]$	N_A	10^{22}
Static relative permitivity	ϵ	11.7
Band gap $[eV]$	E_{gap}	1.15
Temperature $[K]$	T	300

TABLE 3.1: The main input parameters for a thin film Si p/n junction solar cell.

Fig. 3. 3 shows the simulation output for a classical silicon p/n junction solar cell. The parameters like the band gap E_{gap} and the static relative permitivity ϵ were taken from the literature [39]. Doping concentration from donors and acceptors were set to $N_A = N_D$ (moderately doped case). Optical properties were based on absorption coefficients $\alpha(E)$ determined from first

principles shown in Fig. 3. 1. The simulation $J-V$ characteristics predict an efficiency, η, an open circuit voltage, V_{oc} and a short circuit current density J_{sc} as given in the table 3. 2.

J_{sc}	V_{oc}	η
176 A/m^2	0.46 V	6.4 %

TABLE 3.2: Performance of thin film Si solar cell.

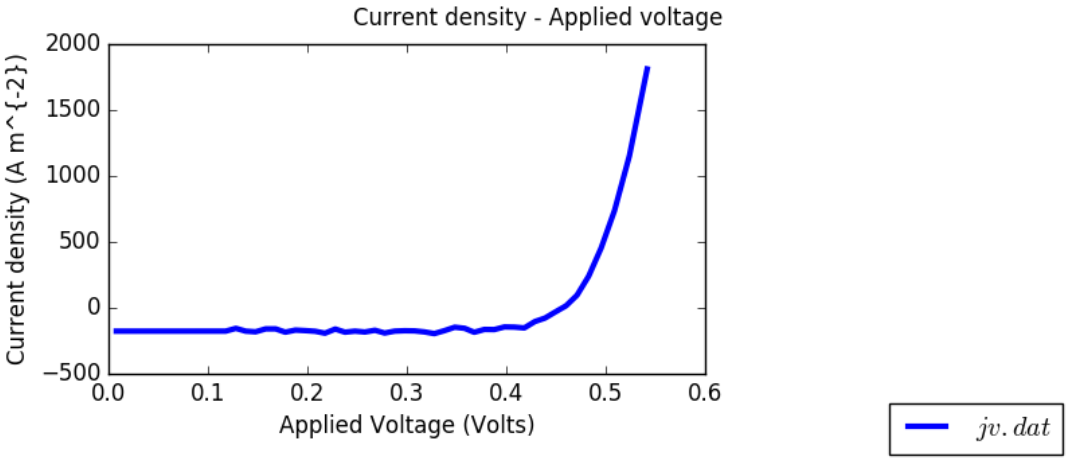


FIGURE 3.3: Simulated $J-V$ characteristics for a silicon p/n-junction solar cell.

If we compare the simulated devices in Chapter 2 and 3, we see a big difference in efficiency between Table 2. 2 and Table 3. 2. The thin film solar cell has poor absorption because the light has a short path-length in the device and the numerical package that we used also includes a more realistic description of the optical and electronic processes inside the solar cell and prediction of a much lower efficiency.

Chapter 4

Plasmonic Nanoparticles

4.1 Introduction

In a nutshell, plasmonics are the interaction between light and free electrons in a metal. The applications of plasmonics include *inter alia* light concentration for solar cells, imaging for medicine and cancer treatment [40]. To explore plasmonics, the dielectric function $\tilde{\epsilon}(\omega)$ needs to be determined before we can explain the optical and thermal properties of the metal.

The dielectric function depends on the frequency ω of light and describes the interaction of light with a solid. It can be measured or determined by using numerical modelling. For more details see ref. [41]. Here we restrict, the size of the nanoparticles to between 1 and 100 nm. The size of the nanoparticles should be smaller than the wavelength of light in order to use the dipole approximation. For more extended objects we would be forced to use a coupled-dipole approach [41] which is beyond the scope of this thesis. These small nanoparticles show strong dipolar excitation in the surface plasmon resonances [42]

In this study, we will use both Drude and Drude-Lorentz theory to compare the resulting model dielectric function with the experimental dielectric function. This will be carried out for Ag and Au nanoparticles of different sizes.

4.2 Dielectric function

Note the conversion from angular frequency ω to the wavelength λ is $\omega = 2\pi c/\lambda$, where c is the speed of light. The imaginary part of the dielectric function $Im(\epsilon)$ describes energy (absorption) losses and the real part of the dielectric function $Re(\epsilon)$ describes the phase shift and reflection of photons. Fig. 4. 1 shows the experimental result of the real part of the dielectric function $Re(\epsilon)$ and the imaginary part of the dielectric function $Im(\epsilon)$ of Au and Ag. $Re(\epsilon)$ part of Au and Ag describes how light interacts with the metal with $Re(\epsilon)$ increasing in magnitude with wavelength, $Im(\epsilon)$ part of Au and Ag describes the losses of energy that comes from the electrons motion and which increases with wavelength [41]. From Fig. 4. 1 we see that of the $Re(\epsilon)$ for both Au and Ag are negative and they are different due to the difference in

their electron density (Au has the higher electron density). The $Im(\epsilon)$ shows dissipation of energy and differences between them and their resonance frequency.

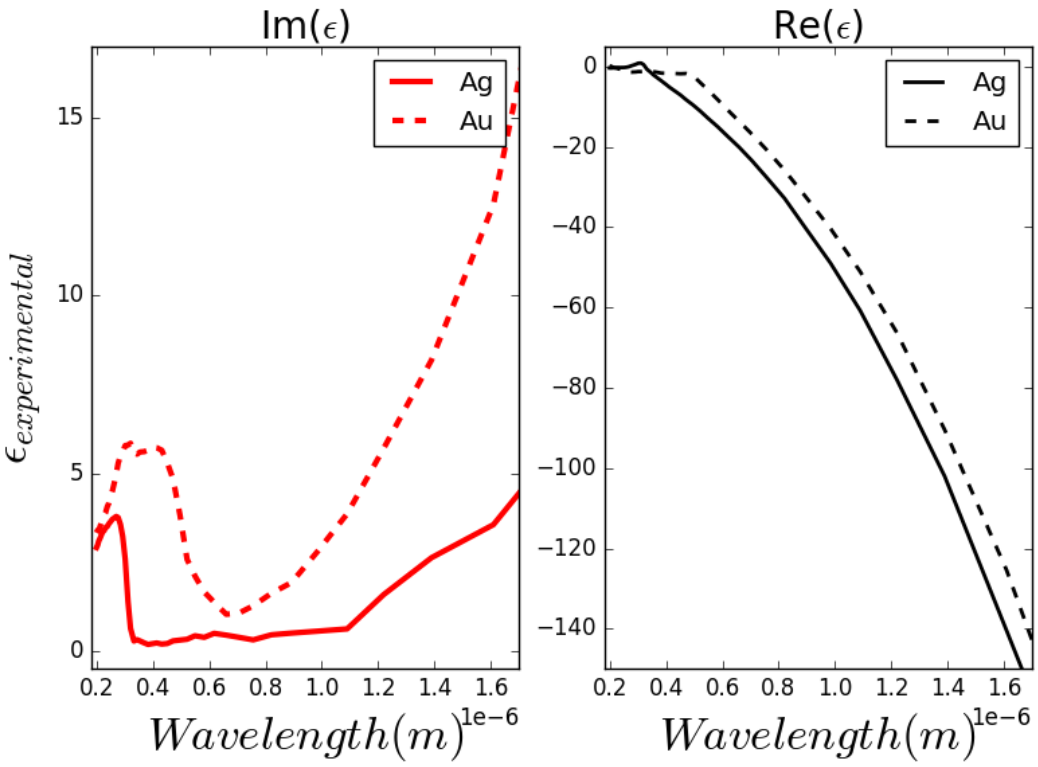


FIGURE 4.1: Experimentally imaginary and real part of the dielectric function ϵ for silver, and gold (experimentally data was obtained from ref. [43]).

4.2.1 Dielectric function Based on the Drude Model

Drude theory is based on a free electron model of a metal. The dielectric function $\epsilon_{Drude}(\omega)$ is given as:

$$\epsilon_{Drude}(\omega) = \epsilon_0 - \frac{\omega_p^2}{\omega + i\Gamma\omega} \tag{4.1}$$

where

$$\omega_p = \sqrt{\frac{n\, e^2}{m\, \epsilon_0}},$$

is the plasma frequency, and e, m are charge and effective mass of free electrons, ϵ_0 is the permitivity of vacuum and n is the electron density. Γ is a damping term proportional to $\frac{v_f}{l}$, where v_f is the Fermi velocity and l is the electron mean free path between two scattering events [41, 44]. The parameters of

Au and Ag are given in the table 4. 1. From the parameters in table 4. 1, the dielectric function with its imaginary and real parts is shown in Fig. 4. 2 as a function of wavelength for Au and Ag.

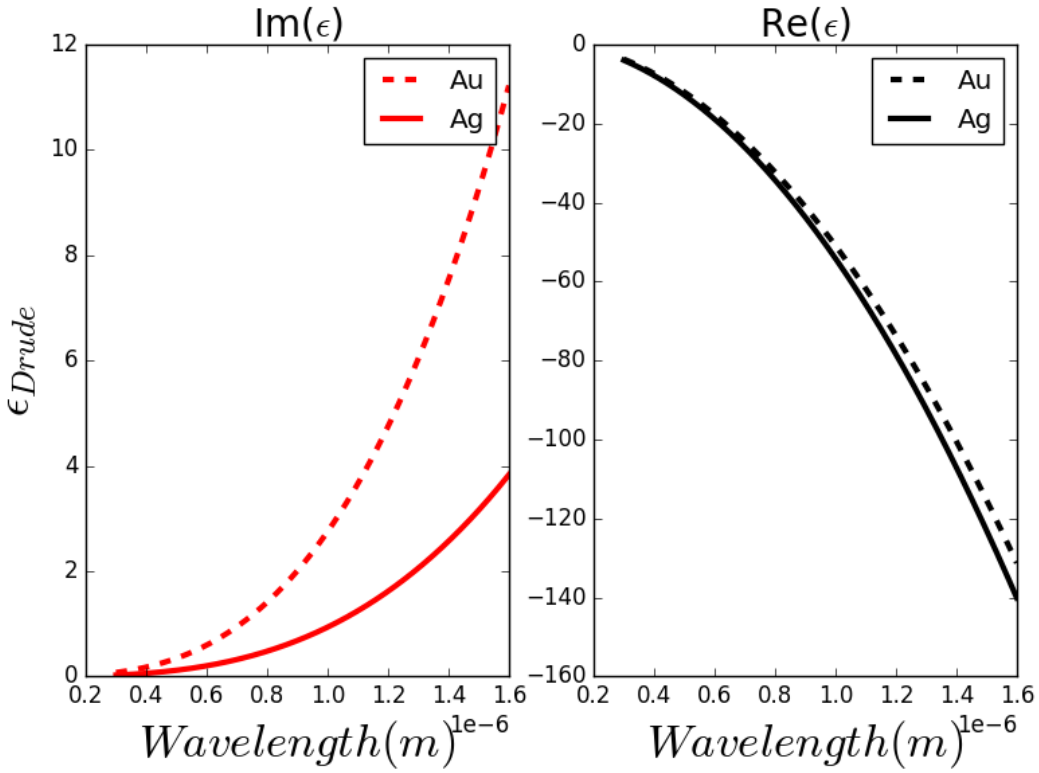


FIGURE 4.2: Imaginary and Real part of the dielectric function for silver and gold by Drude model.

When comparing Figs. 4. 1 and 4. 2, we see that the Drude model gives quite accurate results in the *infrared* region, but for *UV* regions the result is at best an approximation.

4.2.2 Dielectric Function Based on the Drude-Lorentz Model

In order to describe the response of the metals to higher energetic photons, we have to include the transition of electrons from the valance band to the conduction band. To get more accurate results we add inter-band contributions to the Drude-Lorentz model, which f_i, these take account of bound charges in the metal. With a single one of these interband transitions the dielectric functions is given by [40]

$$\epsilon(\omega) = \epsilon_\infty - \frac{\omega_p^2}{\omega^2 + i\Gamma_p\omega} - \frac{f_1\omega_1^2}{(\omega^2 - \omega_1^2) + i\Gamma_1\omega} \tag{4.2}$$

where ϵ_∞ is the dielectric function at infinite frequency, Γ_1 is the Lorentz oscillator damping rate, ω_1 is the Lorentz resonance frequency and f_1 is a weighting factor. Parameters for Au and Ag are given in table 4. 1.

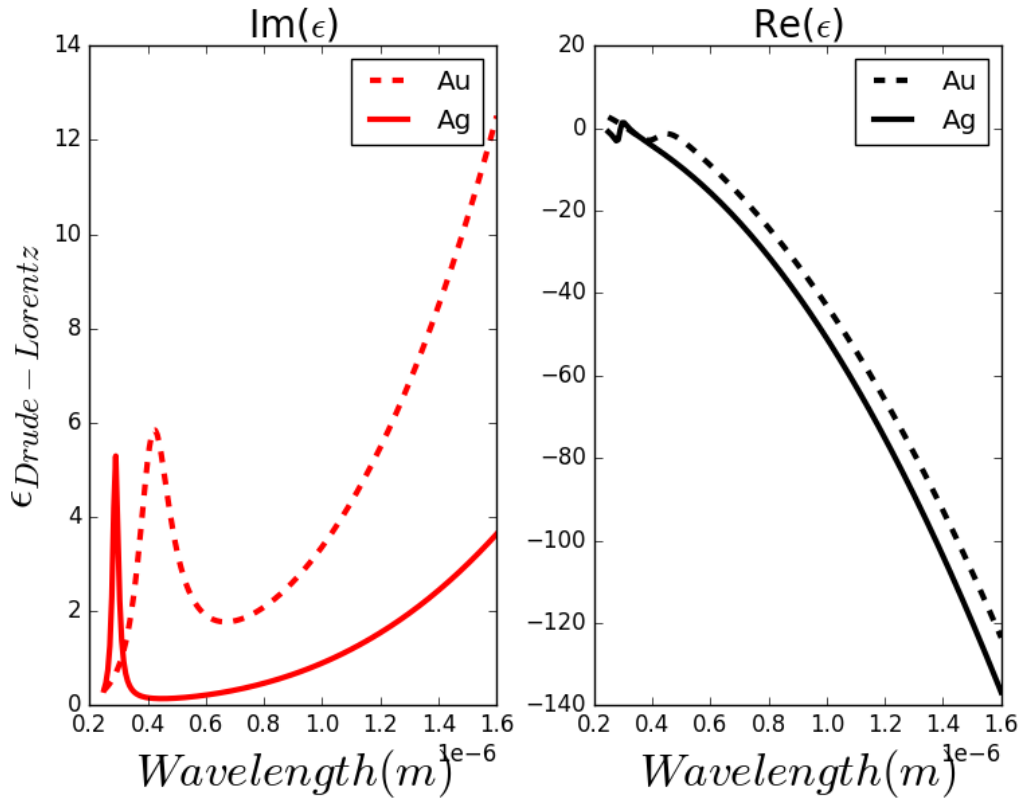


FIGURE 4.3: Imaginary and Real part of the dielectric function for silver and gold using the Drude-Lorentz model. This was plotted using the python code in the appendix A.1.

Parameters	Au	Ag
ω_p [eV]	8.96	9.20
ω_1 [eV]	2.97	4.28
Γ_p [eV]	0.072	0.02
Γ_1 [eV]	0.95	0.34
f_1	1.78	0.428
ϵ_∞	6.88	3.71

TABLE 4.1: The parameters for a Drude-Lorentz model of Au and Ag

When compared to experimental results, the result from the Drude-Lorentz model (Fig. 4. 3) is a more accurate result, especially in the UV region.

Note that $\tilde{\epsilon}(\omega)$ can also be determined from *ab-initio* methods based on density functional theory and the data obtained from these simulation can also be used to generate the parameters for the Drude-Lorentz model [45]

4.3 Scattering and Absorption by Metal Nanoparticles

Scattering and absorption by plasmonic nanoparticles play a significant role for thin film solar cells which we will explain in the next chapter. Here we picked Ag with a resonance frequency in the *ultraviolet* range and Au that resonance frequency in the *visible* region and calculate the corresponding scattering and absorption cross-sections.

Spherical Case

Let us look at spherical nanoparticles Nps with radius, r, embedded in a homogeneous dielectric matrix (this model was first examined by Mie[41, 46]) where the radius of the spherical nano-particle will be much smaller than the wavelength of the scattered and absorbed light. Then the absorption and scattering cross-sections are obtain from the polarisability, α as follows [41]

$$\sigma_{scatt} = \frac{k^4}{6\pi\epsilon_0^2} \mid \alpha \mid^2 \tag{4.3}$$

and

$$\sigma_{abs} = \frac{k}{\epsilon_0} Im[\alpha] \tag{4.4}$$

respectively. The polarisability α of a spherical particle is given by:

$$\alpha = 4\pi\epsilon_0 r^3 \frac{\epsilon(\omega) - \epsilon_m}{\epsilon(\omega) + 2\epsilon_m} \tag{4.5}$$

where k is the wavevector in the medium and ϵ_m is the dielectric constant of the surrounding medium, [14, 47, 48]. We considered only the case of spherical 3D nanoparticles, because lower-dimensional systems do not seem to be of any practical use for plasmon enhanced solar cells.

From Eq. 4. 5 the resonance frequency shifts with the dielectric constant of the medium (see Fig. 4. 4). Here the radius of nanoparticles were fixed at 30 nm. Fig. 4. 4 shows the scattering and absorption cross-section of Ag with different media.

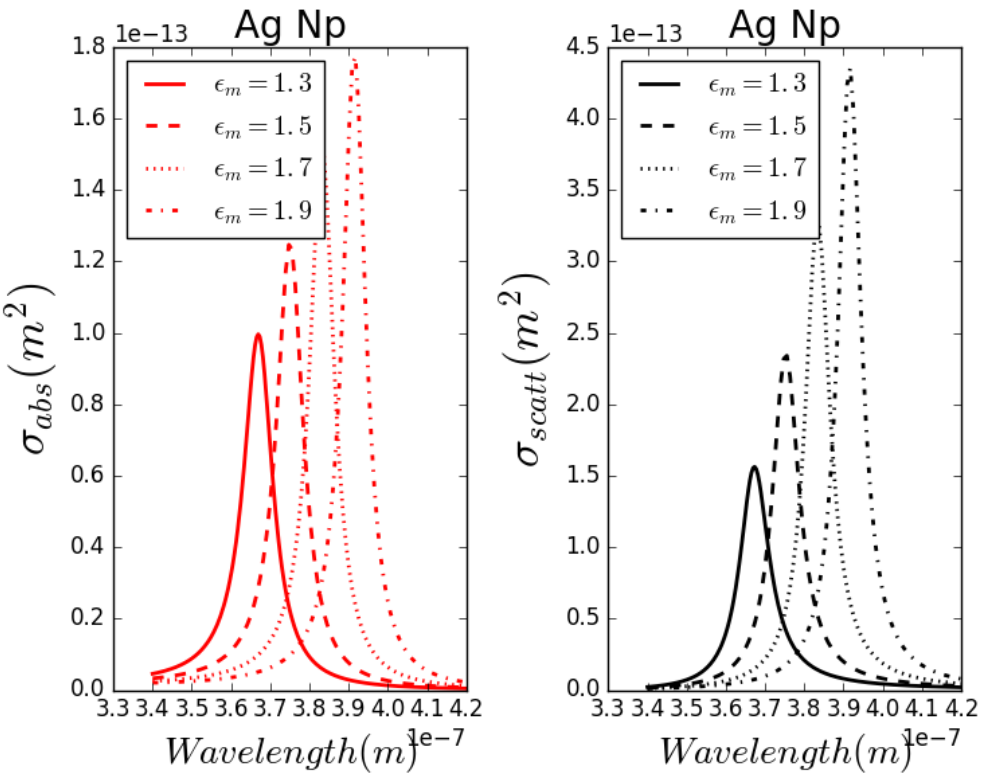


FIGURE 4.4: Shifted scattering and absorption cross-section of Ag Np by different media. ($r = 30\ nm$)

Furthermore the cross-section varies with radius, r, of the nanoparticles. We see that, σ_{scatt} scales with r^6 and σ_{abs} scales with r^3. Therefore, while σ_{abs} is dominant for Nps with small radii and, σ_{scatt} is dominant for Nps with big radii. This is shown in Fig. 4. 5. We see that absorption is higher than scattering at $r = 30\ nm$ as expected from eqs. 4. 3 and 4. 4 for Nps with small radius r. But that should be opposite for Nps with large radius r. For the Ag Np in Fig. 4. 5 at 28 nm the scattering and absorption cross-sections are about equal and for larger particles, the scattering becomes dominant, while for the Au Np at 64 nm they are equal and for larger particles the scattering becomes dominant. We should point out that the radius of the spheres should not be larger than the incident light wavelength, because the electromagnetic field that surrounds the Nps should be homogeneous [49–51]. If the Nps are larger we would need to use a different model and the electromagnetic field of the light may be focused on a part of the nanoparticle and not be homogeneous.

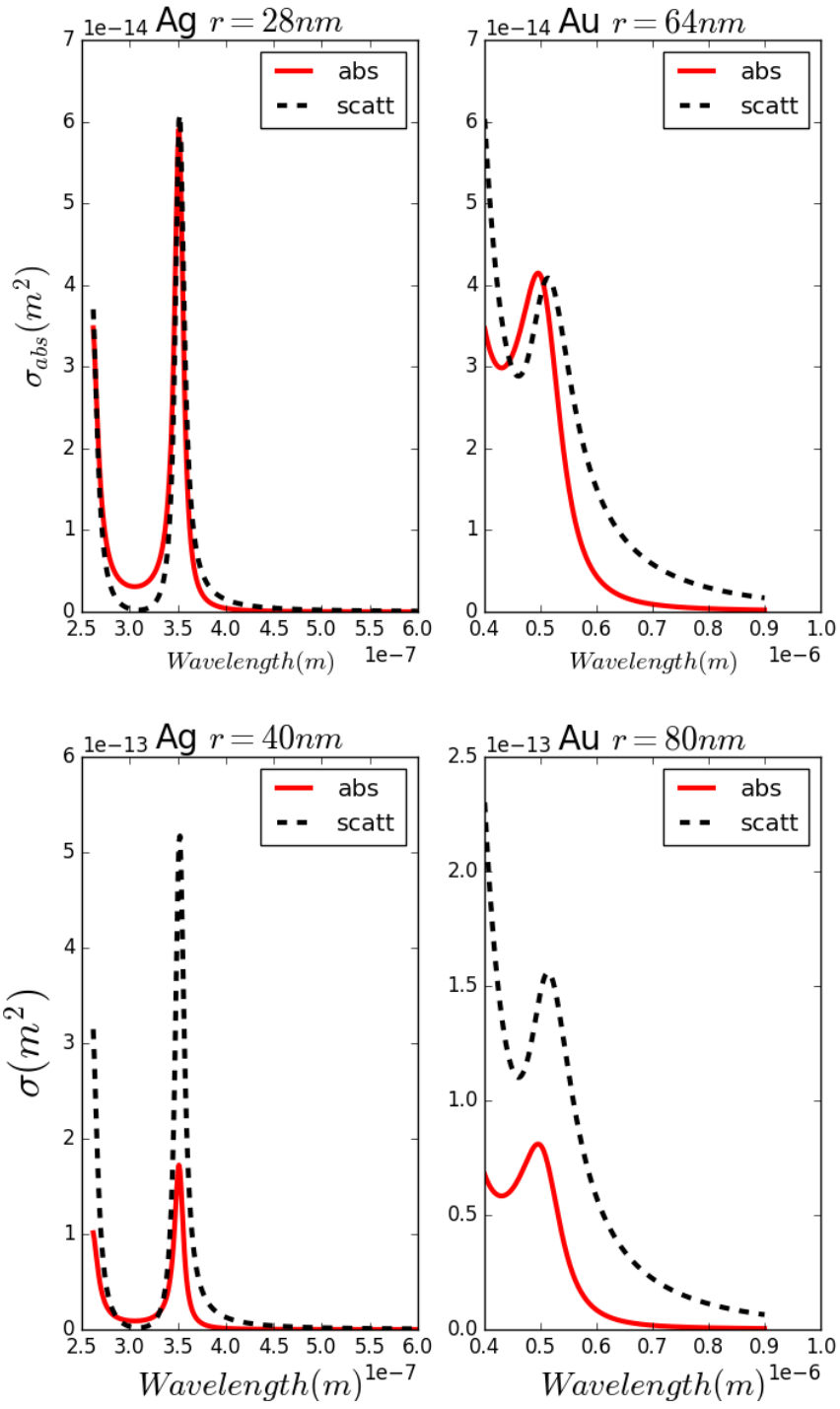


FIGURE 4.5: Scattering and absorption cross-section for Au and Ag Nps as a function of the wavelength, and for various radii of the metallic Nps. The dielectric function of the surroundings is $\epsilon_m = 1.8$ which is corresponding to ice. This was plotted using the python code in the appendix A.2.

Ellipsoidal Case

So far, we have just assumed spherical nanoparticles and we have analyzed their optical properties. In experimental studies the metallic Nps are often not spherical but look like ellipsoids see Fig. 4. 6.

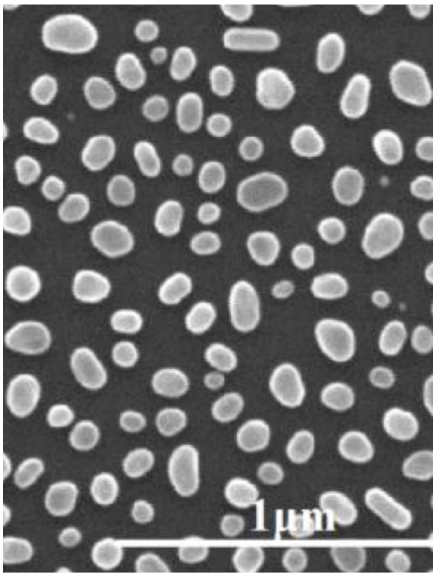


FIGURE 4.6: SEM images of ellipsoidal Ag Nps. The figure was obtained from ref. [52].

In this section we want to study small and ellipsoidal metal nanoparticles and compare the results to the spherical case. The polarisability of ellipsoidal Nps is given by

$$\alpha = V \frac{\epsilon(\omega) - \epsilon_m}{\epsilon(\omega) + \frac{1-L_i}{L_i}\epsilon_m} \tag{4.6}$$

where $V = \frac{4\pi}{3}abc$ (a,b and c are the radii of axes) is the volume of the ellipsoidal nanoparticle, and L_i is a geometrical factor with $i = x, y$ or z. Two special ellipsoidal shapes are the prolate and the oblate ellipsoid. As can be seen from Fig. 4. 7 for the oblate ellipsoid the relationship between coordinates is $x = y > z$ and for the prolate ellipsoid is $z > x = y$.

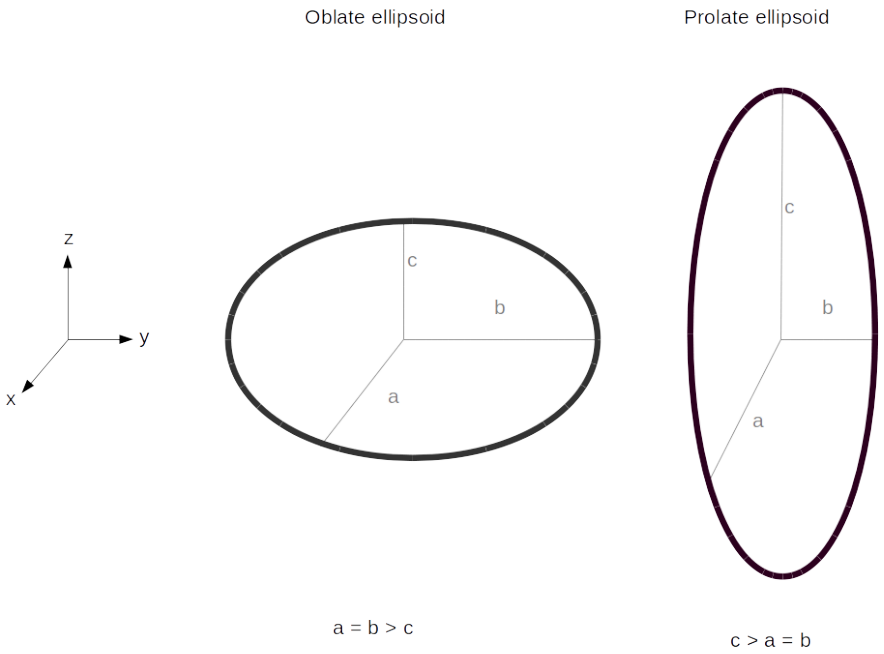


FIGURE 4.7: Schema of prolate and oblate ellipsoid.

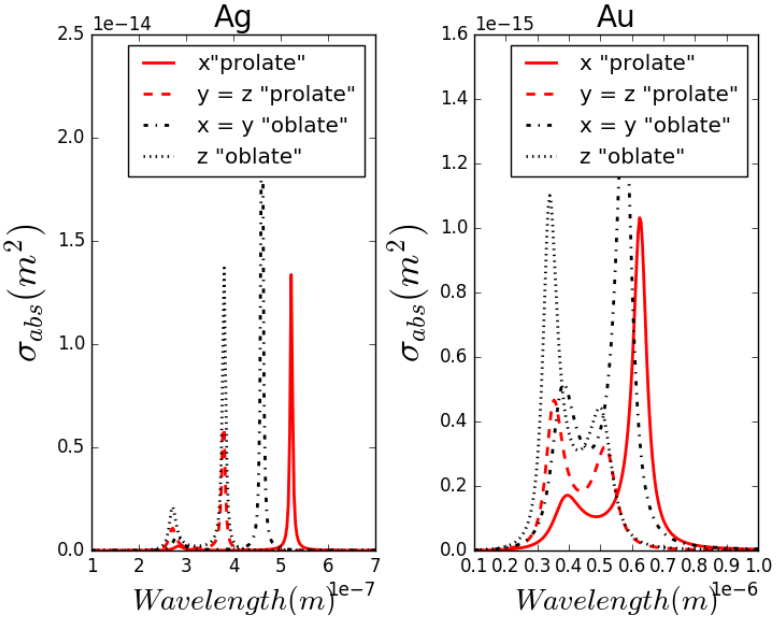
Fig. 4. 7 shows simulation result the prolate and the oblate ellipsoids that will be considered as possible metal Nps in our study. The geometric factor along the x direction, L_x, for the prolate ellipsoidal and oblate ellipsoidal nanoparticles are given as, [53],

$$L_{x,prolate} = \frac{1-e^2}{e^2}\Big(-1+\frac{1}{2e}ln\frac{1+e}{1-e}\Big) \quad and \quad L_{x,oblate} = \frac{1-e^2}{e^2}\Big(-1+\frac{1}{2e}ln\frac{1+e}{1-e}\Big) \tag{4.7}$$

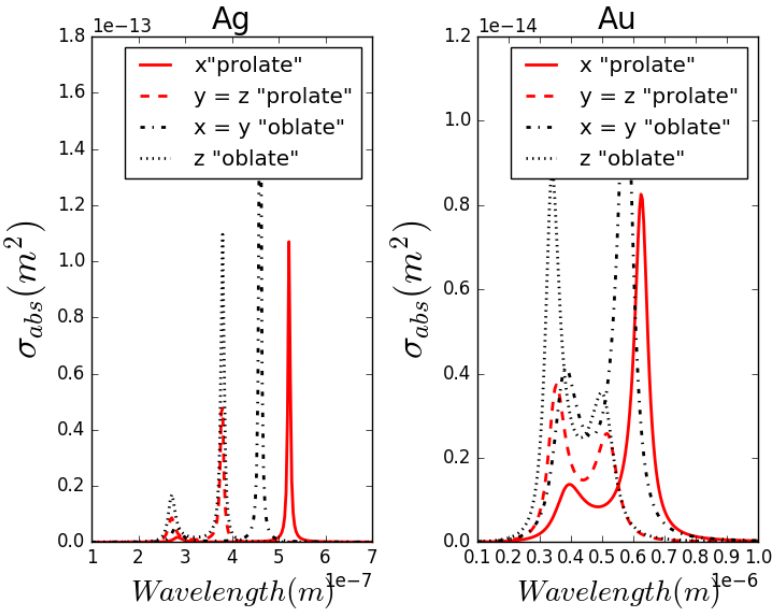
Where $e = \sqrt{1-\frac{c^2}{a^2}}$. The other geometric factors L_y and L_z in the y and z direction are related to L_x, as follows

$$\begin{aligned} L_y = L_z = (1-L_x)/2 > 1/3 > L_x \quad &\text{for} \quad prolate \\ L_z = 1-2L_x > 1/3 > L_x = L_y \quad &\text{for} \quad oblate \end{aligned} \tag{4.8}$$

We can now use Eqs. 4. 3, 4. 4 and 4. 6, to determine the absorption cross-section for both prolate and oblate ellipsoids. Fig 4. 8 shows the absorption cross-sections for Ag and Au prolate and oblate nano-ellipsoids perpendicular to different axes.



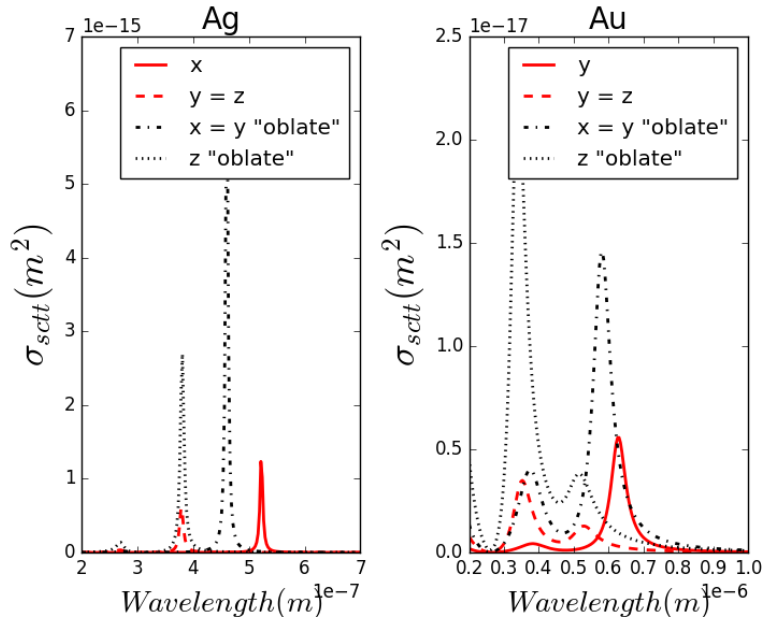
(A)



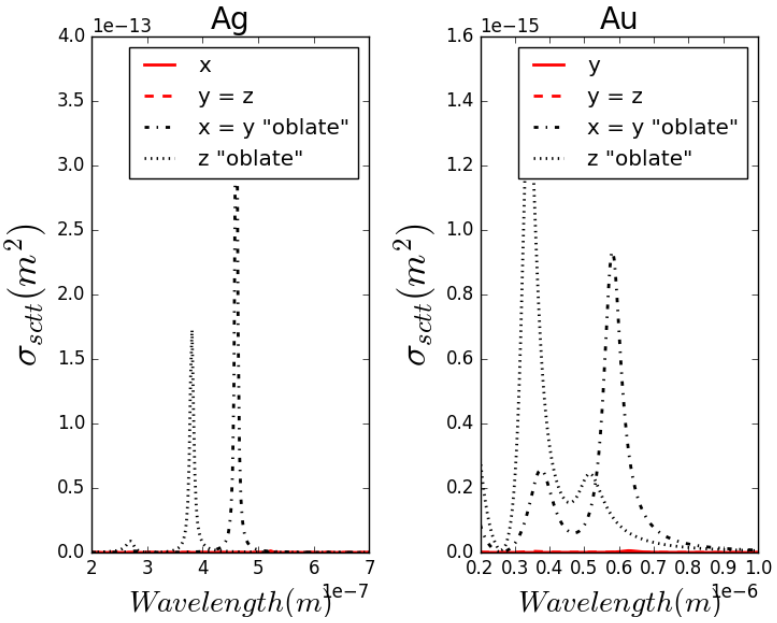
(B)

FIGURE 4.8: Absorption cross-section of Ag and Au prolate and oblate ellipsoids. (A) In the prolate case; a, b and c are 24 nm, 12 nm and 12 nm, respectively and in the oblate case; a, b and c are 24 nm, 24 nm and 12 nm, respectively and (B) in prolate case; a, b and c are 48 nm, 24 nm and 24 nm, and in oblate case; a, b and c are 48 nm, 48 nm and 24 nm, respectively. $\epsilon_m = 2.25$.

From Eqs. 4. 4 and 4. 6, we have plotted the absorption cross-section for both the prolate and the oblate ellipsoid. Fig 4. 9 shows the scattering cross-section for Ag and Au prolate and oblate nano-ellipsoids in different directions.



(A)



(B)

FIGURE 4.9: Scattering cross-section of Ag and Au prolate and oblate ellipsoids. (A) In the prolate case; a, b and c are 24 nm, 12 nm and 12 nm, respectively and in the oblate case; a, b and c are 24 nm, 24 nm and 12 nm, respectively and (B) in prolate case; a, b and c are 48 nm, 24 nm and 24 nm, and in oblate case; a, b and c are 48 nm, 48 nm and 24 nm, respectively. $\epsilon_m = 2.25$.

Compared to the spherical case, the cross-sections for the ellipsoidal case vary with the size of Nps and show the same behaviour as a function of increasing size for absorption and scattering cross-section see Fig 4. 8 and 4. 9.

4.3.1 Heat generated by plasmonic Nanoparticles

When plasmonic Nps are embedded in a medium that is illuminated by light, they will generate heat when the photons are absorbed. We just used the simplest possible model to describe heating.This property of plasmonic Nps will decrease the solar cell's efficiency but it is beneficial for other applications such as medicine [54]. For this section, we will only use the Au Nps but the same simulation can be done for other metals as well.

If we assume that there is no the phase transformation, the temperature distribution around the Nps is determined by the general heat transfer equation:

$$p(\mathbf{r})c(\mathbf{r})\frac{dT(\mathbf{r},t)}{dt} = \nabla k(r)\nabla T(\mathbf{r},t) + Q(\mathbf{r},t), \tag{4.9}$$

where $T(\mathbf{r},t)$ is the local temperature, which depends on the coordinate, $\mathbf{r}$, and time t. $p(\mathbf{r})$, $c(\mathbf{r})$, $k(\mathbf{r})$ and $Q(\mathbf{r},t)$ are the mass density, specific heat, thermal conductivity, and an energy source Q term that stems from light dissipation in the Nps. The energy source Q from the dissipation of light in the Nps is related to the absorption cross section, and for spherical particles we obtain [50]

$$Q = \frac{\omega}{8\pi}E_0^2 \mid \frac{3\epsilon_m}{2\epsilon_m + \epsilon_{NP}} \mid^2 Im(\epsilon_{NP}), \tag{4.10}$$

where E_0 is the amplitude of the incoming radiation, ϵ_m is the dielectric constant of the surround medium, and ϵ_{NP} is the dielectric function of the Np. The corresponding intensity is given by

$$I(t) = I_0 = cE_0^2\sqrt{\epsilon_m}/8\pi \tag{4.11}$$

The analytical result of Eq. 4. 9 under steady-state conditions is easily obtained for the local temperature profile on and surrounding a single Np is

$$\Delta T(\mathbf{r}) = \begin{cases} \frac{V_{NP}Q}{4\pi k_0 R_{Np}} & \text{for} \quad r = R_{Np} \\ \frac{V_{NP}Q}{4\pi k_0 r} & \text{for} \quad r > R_{Np} \end{cases} \tag{4.12}$$

where ΔT is the temperature difference relative to the initial state without illumination, r is the distance from the center of the spherical Np, k_0 is the thermal conductivity of the surrounding medium, and V_{NP} is the Np volume. From the Eqs. 4. 10, 4. 11 and 4. 12 we see that the temperature difference is proportional to the photons flux intensity (see Fig. 4. 10). Fig. 4. 10 shows the temperature difference as a function of the intensity.

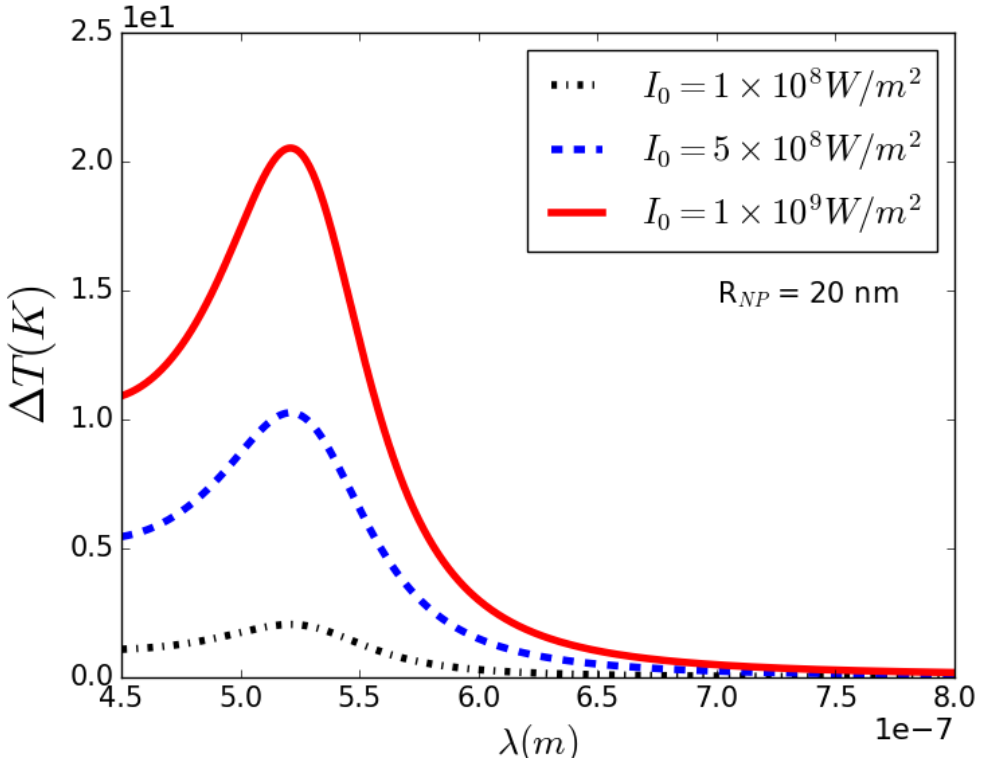
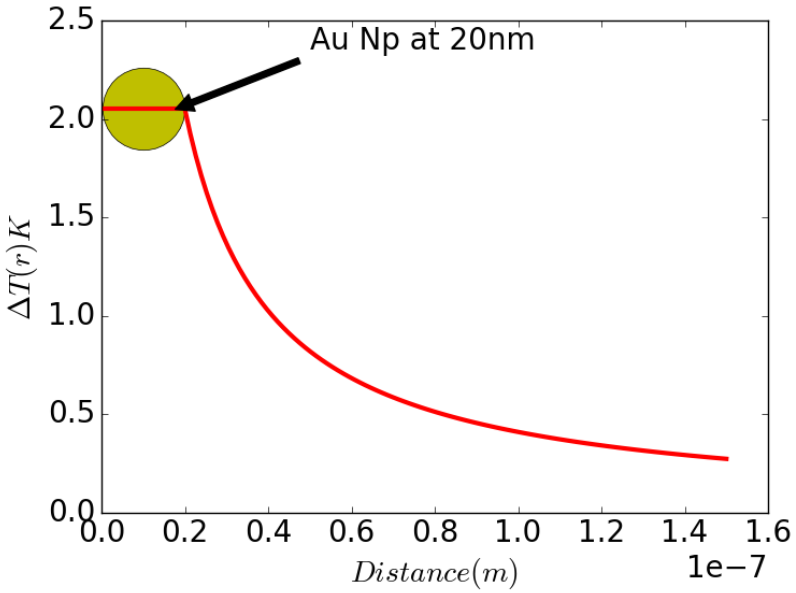
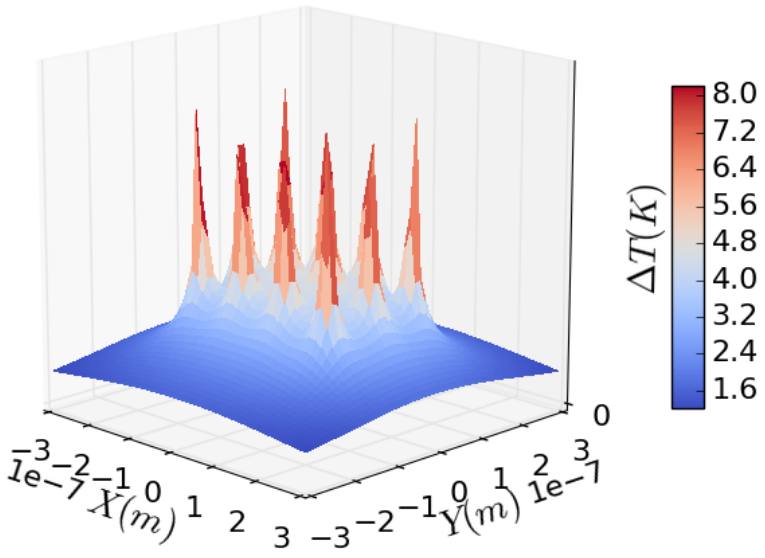


FIGURE 4.10: Temperature changes for different flux intensities as a function of the wavelength in an environment with $\epsilon_m = 1.8$. The radius r, of the Np is 20 nm.

The fig. 4. 10 shows us the plasmon resonance wavelength, which is clear in the figure as $\lambda = 520$ nm. The temperature change on the Np and its surroundings for one 20 nm Au Np can then be determined from the equations given above. The results are shown in Fig. 4. 11 (a) where the temperature change on and around the Au Np is plotted as a function of distance from the nanoparticle. In fig. 4. 11 (b) is a map of the temperature change in a 2 dimensional plane sliced from a 3 dimensional model where 12 Nps (3x4) sit on this plane. The distance between the Nps is 80 nm.



(A)



(B)

FIGURE 4.11: (a) Temperature change as a function of distance and (b) temperature change for an array of 3x4 Nps as a function of x, y coordinates ($R_{Np} = 20\ nm$). The initial flux intensity is $I_0 = 1 \times 10^8\ W/m^2$. This was plotted using the python code in the appendix A.3.

From Eq. 4. 12 we can see the temperature changes from the surface of the Np into the bulk with radius of the Np,R_{Np}, as follows:

$$\Delta T \sim R_{Np}^2 \tag{4.13}$$

Now we will look at the temperature drops from the surface of the nanoparticle in to the bulk. Fig. 4. 12 shows the temperature gradient for one and many Nps with two different radii. This is to illustrate Eq. 4. 13 above.

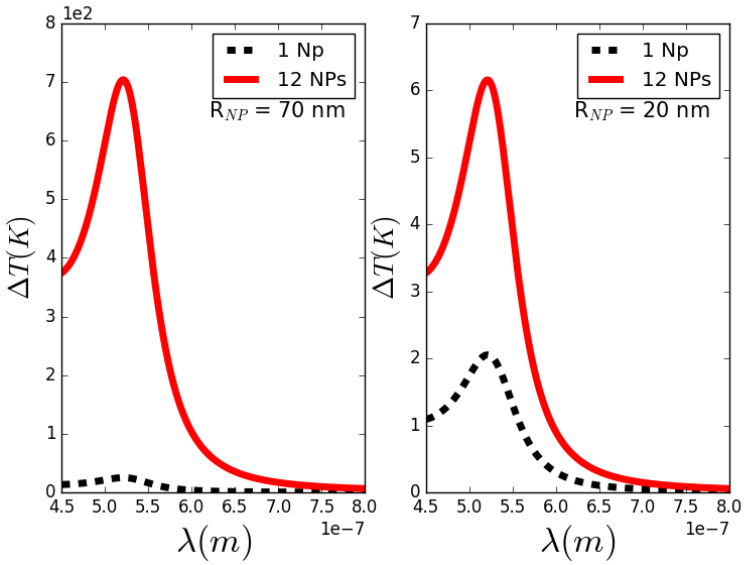


FIGURE 4.12: Temperature gradient of one and 12 Nps as a 3x4 array as a function of wavelength at $R_{Np} = 70\ nm$ and $R_{Np} = 20\ nm$. The distance between Nps is 100 nm and the initial flux intensity is $I_0 = 1 \times 10^8\ W/m^2$.

Note that we only considered the heating caused by higher concentrations of plasmonic nanoparticles other heating effects are secondary in this respect.

Chapter 5

Performance Enhancement of Solar Cells by Plasmonics Nanoparticles

5.1 Introduction

In this section we will simulate the increase in the efficiency of a solar cell using embedded plasmonic nanoparticles. We will be considering thin film solar cells, they are relatively cheaper than the conventional solar cells and they are easier to fabricate. Furthermore because they are thinner there is less charge carrier recombination than in a conventional solar cell. Their main disadvantage however is that there is insufficient absorption of light thus reducing their efficiency.

Fig. 5. 1 shows the structure of random Nps in such a thin film solar cell, (see ref. [55, 56]).

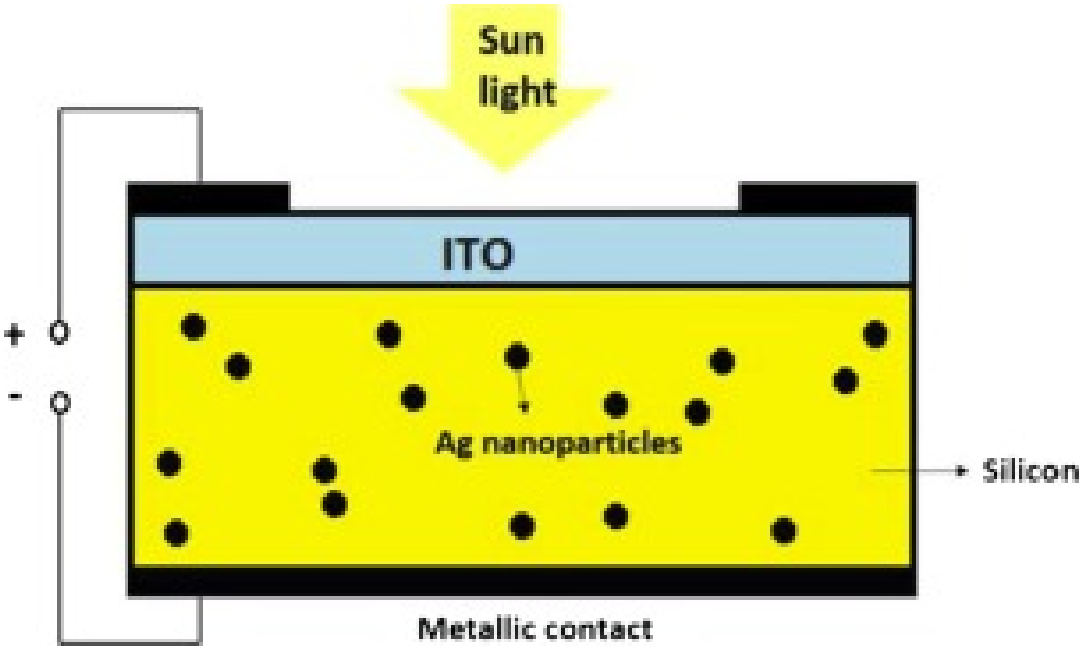


FIGURE 5.1: Configuration of random *Au* Nps in the solar cell (this figure was obtained from ref [57]).

The numerical and experimental method that we will use is the direct embedding of metal Nps, such as Au or Ag, into the solar cell to enhance light collection. Once embedded the Nps will cause extra light absorption. This leads to the creation of additional $electron - hole$ pairs within the active layer of solar cells and therefore to an extra current density.

The key will be the determination of the effective absorption coefficients of bare Si solar cells due to the deposition of metal Nps. On that basis we will show how to estimate the efficiency of these augmented solar cells.

5.2 Light Trapping by Metal Nanopatricles

We have already calculated the optical properties of metal Nps in previous chapters, such as the dielectric function, absorption cross-section and scattering cross-section. The concentration, shape and size of Nps plays a significant role in these processes, which was partly demonstrated in the previous chapters.

In the following Fig. 5. 2 we will plot the extinction cross-section as a function of the nanoparticle radius and the dielectric function of spherical Ag and Au Nps in a frequency range of interest for photovoltaics. Extinction cross-sections σ_{ext} are given by

$$\sigma_{ext} = \sigma_{abs} + \sigma_{sct} \tag{5.1}$$

where σ_{abs} and σ_{sct} are absorption and scattering cross-sections respectively. Fig. 5. 2 shows the extinction cross-section of Au and Ag as a function of radius. Evidently, the Ag surface resonance is at 350 nm which is in the UV range, and the values are higher than for Au, where the surface resonance is at 500 nm in the visible range.

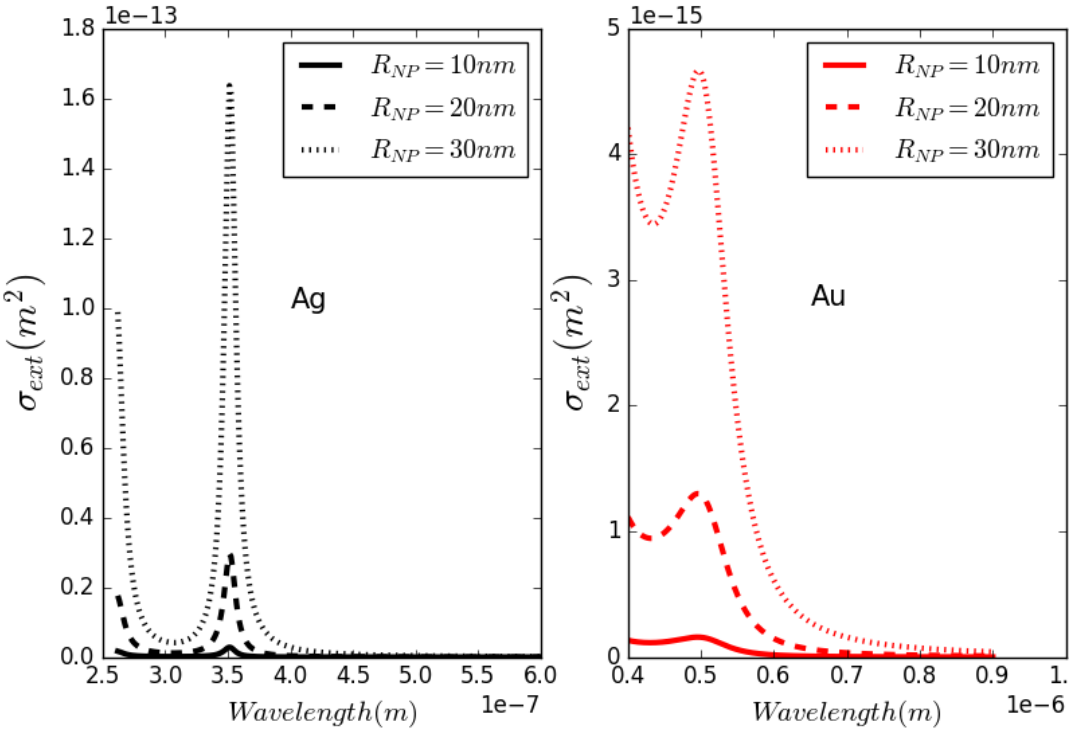


FIGURE 5.2: Extinction cross-section of Au and Ag as a function of radius.

Note that the dielectric function, ϵ of spherical Au and Ag is given by

$$\epsilon(\omega) = \epsilon_\infty - \frac{\omega_p^2}{\omega^2 + i\Gamma_p\omega} - \frac{f_1\omega_1^2}{(\omega^2 - \omega_1^2) + i\Gamma_1\omega} \tag{5.2}$$

based on the Drude-Lorentz theory. This has been derived in the previous chapter, where values for the different parameters are indicated.

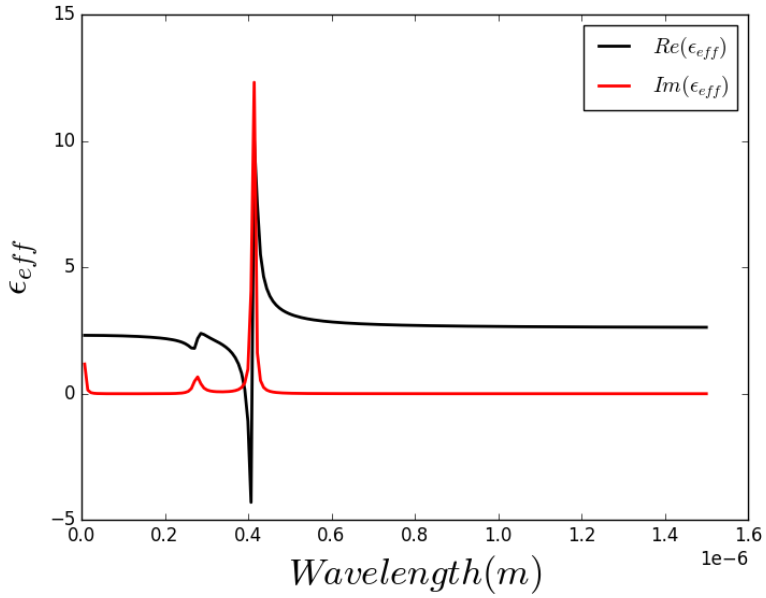
Now let us assume that the Nps are embedded inside a thin film Si solar cell forming a composite. Some of the best ways to get information about the optical properties of a composite material are first principle methods or experimental results; however we will use effective medium theory in this chapter. Effective medium theory as developed by Maxwell-Garnett to calculate the effective dielectric function ϵ_{eff} of a composite [57, 58].

We assume that N spherical Nps are distributed randomly across the silicon solar cell. Then the effective dielectric function

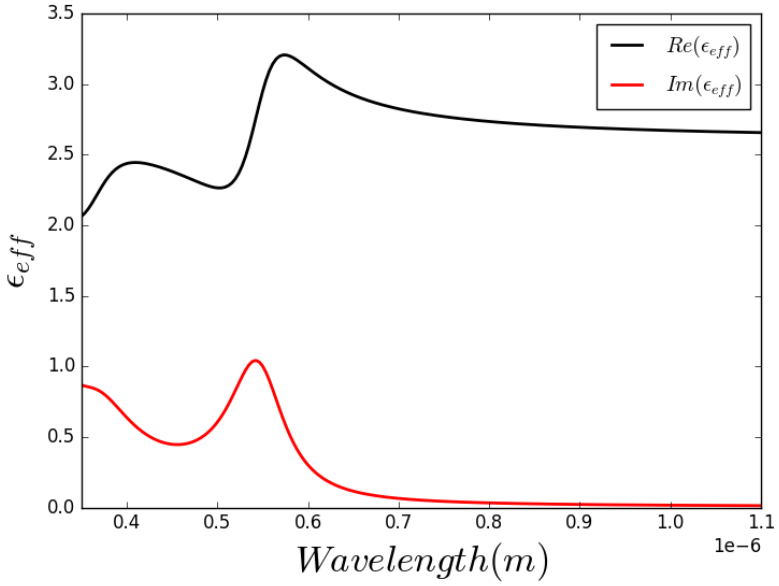
$$\epsilon_{eff} = \frac{\epsilon(1-f)^4}{(1+2f)^2}\left(\frac{1+\frac{2f_s(\epsilon_s-\epsilon)}{(\epsilon_s+2\epsilon)}}{1-\frac{f_s(\epsilon_s-\epsilon)}{(\epsilon_s+2\epsilon)}} + i2f_sk^3a^3\left|\frac{\frac{\epsilon_s-\epsilon}{\epsilon_s+2\epsilon}}{1-\frac{f_s(\epsilon_s-\epsilon)}{\epsilon_s+2\epsilon}}\right|^2\right) \tag{5.3}$$

where ϵ is the dielectric function of the medium, ϵ_s is the dielectric function of

the metal Nps, f_s is the the filling fraction of the metal in the composite which is proportional to the number of the metal Nps N, k is the wavenumber, and a is the radius of the Nps. Fig. 5. 3 shows the effective dielectric function for a typical $Si - Ag$ and $Si - Au$ composite material. It is quite obvious that Ag and Au Nps have different optical behaviors when embedded into silicon as we can see from Fig. 5. 3 [57].



(A)



(B)

FIGURE 5.3: (a) Real and imaginary part of effective dielectric function of $Si - Ag$ composite material and (b) Real and imaginary part of effective dielectric function of Si-Au composite material ($R_{np} = 10\ nm$ and $f_s = 0.05$).

5.3 Silver and Gold Nanoparticles Embedded Randomly in Silicon

Now we will study the enhancement of the efficiency of thin film Si solar cells. In order to calculate the corresponding current density we first have to determine the absorption coefficient of the composite material.

Optical Properties of Silicon

The absorption coefficient and the dielectric function of bare bulk Si may be obtained as follows: The absorption coefficient of bulk Si is calculated from the *k*-selection rule here, given by [59]

$$\alpha(\omega) = 0.0287 exp[2.72(\hbar\omega - E_g)] \tag{5.4}$$

where $\hbar\omega$ is the energy of an incident photon which is $> 1.5\ eV$ for this condition, and E_g is the band gap of silicon. We can plot this absorption coefficient of bare silicon (Eq. 5. 4) and we can compare it to silicon with Ag or Au Nps embedded, the results follow,

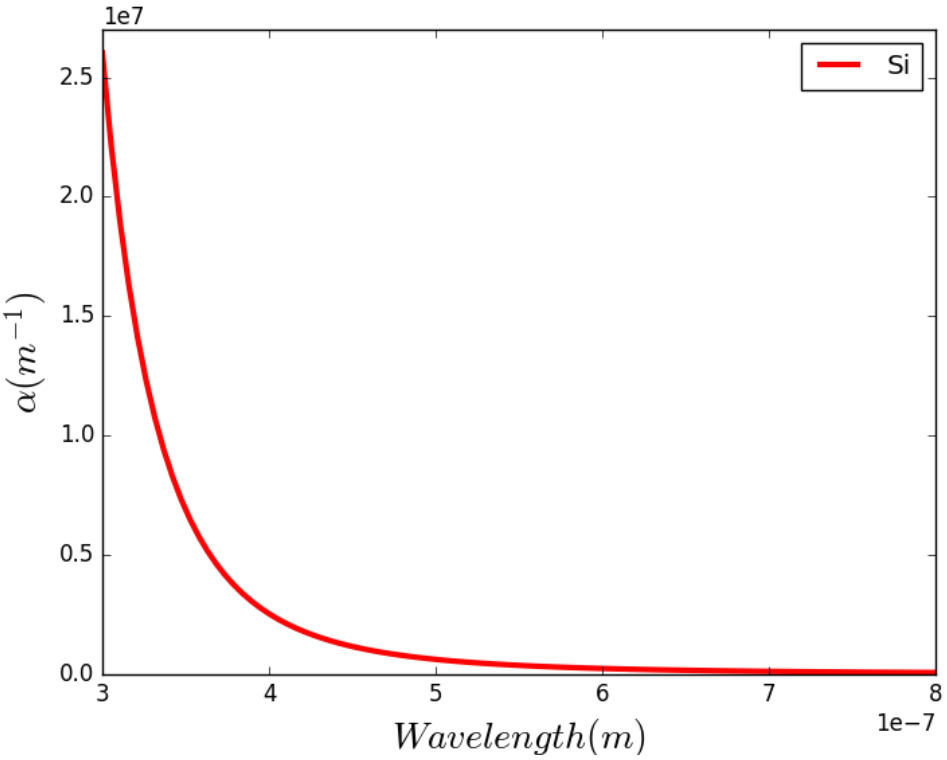


FIGURE 5.4: Absorption coefficient of bulk silicon.

We have also absorption coefficient data from *ab-initio* for a bulk silicon in Chapter 3. Fig 3. 2. It is also useful to know the complex dielectric function of the bare bulk Si as well, which is shown in the Fig. 5. 5.

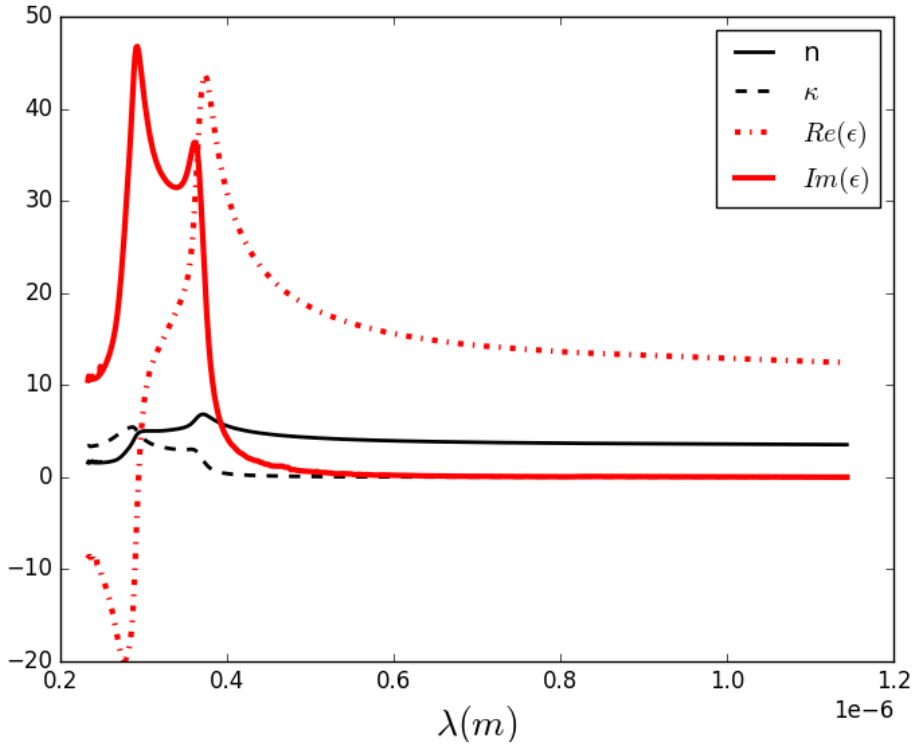


FIGURE 5.5: Imaginary and real part of dielectric function and refractive index of bare Si [60].

5.4 Optical properties of Composite Material

The absorption coefficient of a composite material such as $Si - Ag$ and $Si - Au$ may be calculated from the dielectric function or the complex refractive index. The relationship between the refractive index and the dielectric function was determined in the previous chapter. Using this relationship, we can determine the absorption coefficient by taking the square root of the dielectric function and then determining α from

$$\begin{aligned} \alpha(m^{-1}) &= \frac{4\pi\kappa}{\lambda} \\ &or \\ \alpha(m^{-1}) &= 4\pi Im(\epsilon_{eff})/\lambda \end{aligned} \tag{5.5}$$

where is λ is mean free path [29]. The absorption coefficient with and without Nps is shown in Fig. 5. 6.

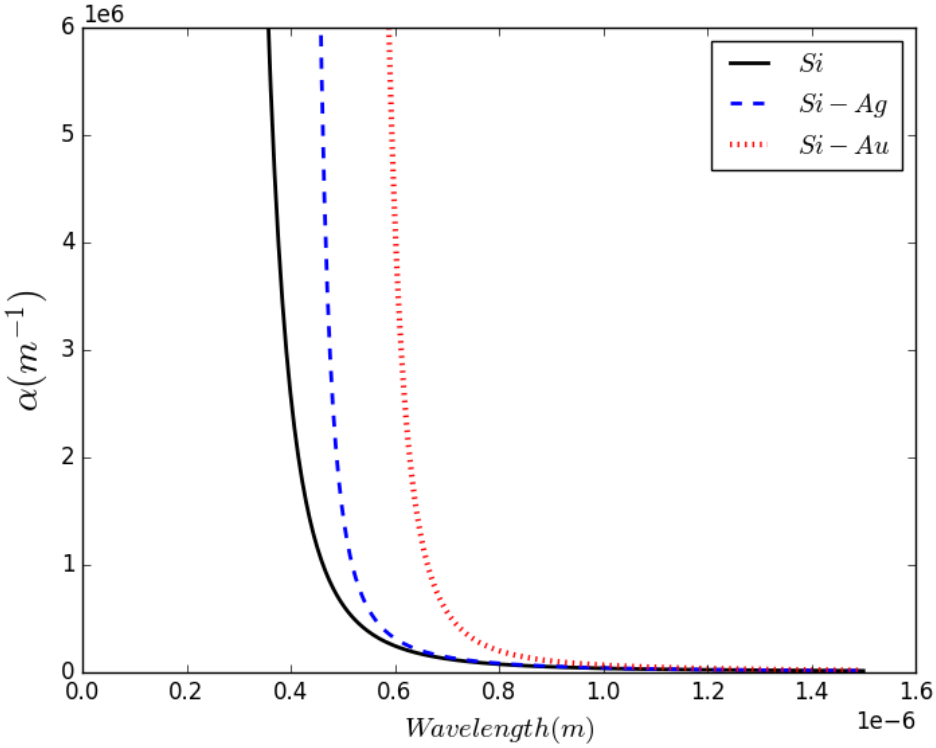


FIGURE 5.6: Absorption coefficient of bare bulk silicon, silicon with Ag Nps, and silicon with Au Nps.

Fig. 5. 6 we can see the enhancement of optical absorption for both $Si - Ag$ and $Si - Au$ in the visible region.

Now we will look at the absorbance A of this composite structure. This is related to the amount of photons absorbed by the structure, which are extracted as current by an external circuit attached to the solar cell.

A also depends on the effective medium, it is given by [61]

$$A = 1 - exp(-\alpha(\lambda)L) \tag{5.6}$$

Here L is the thickness of the absorbing layer. Fig. 5. 7 shows the absorbance for $Si - Ag$ and $Si - Au$ Nps composite materials.

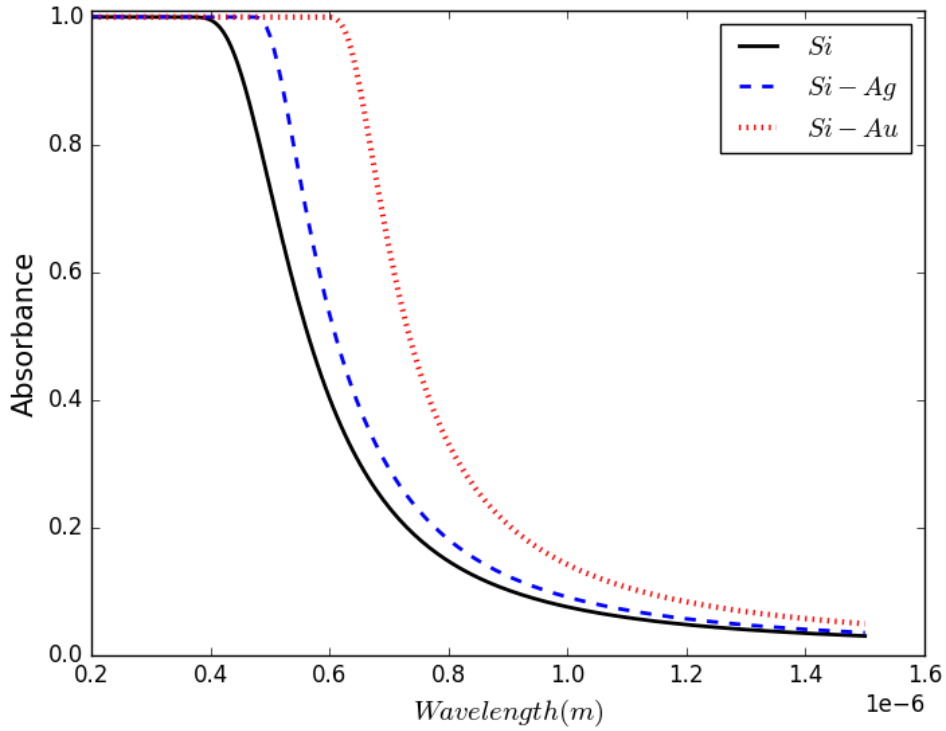


FIGURE 5.7: Absorbance of composite material (a) silicon with spherical gold Nps and (b) silicon with spherical silver Nps (here f_s = 0.05, R_{np} = 10 nm and $L = 1\ \mu m$).

The absorption coefficient can be determined in the case of spherical and small Nps, using the approximate expression [62]

$$\alpha(m^{-1}) = \frac{8.88}{\lambda}\sqrt{-Re\epsilon_{eff} + \sqrt{Re\epsilon_{eff}^2 + Im\epsilon_{eff}^2}} \tag{5.7}$$

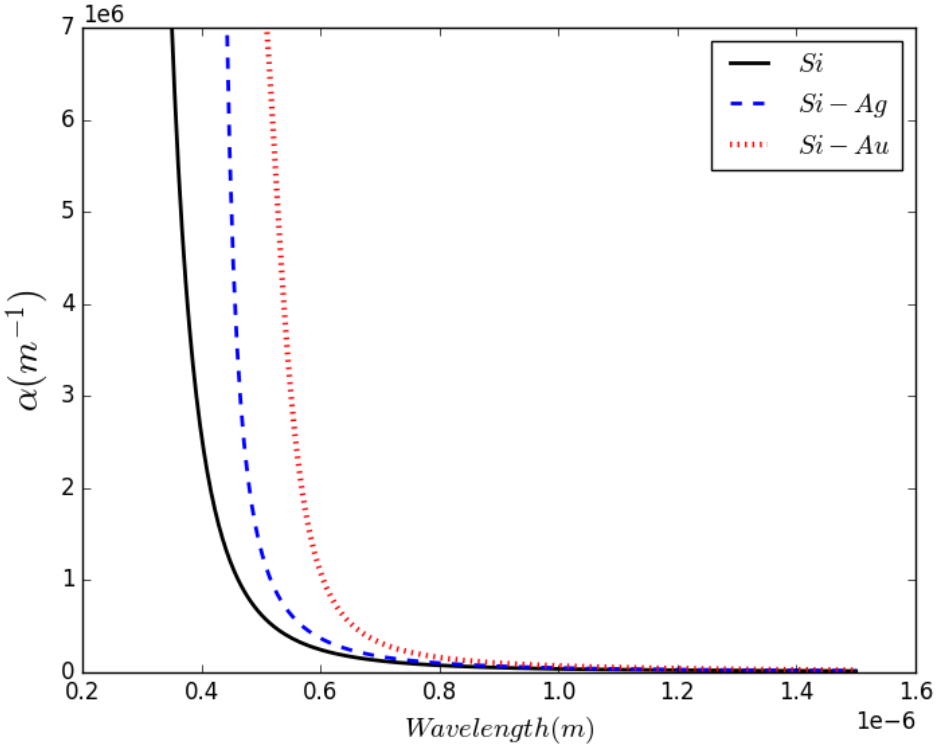


FIGURE 5.8: Absorption coefficient of bare bulk silicon, silicon with Ag Nps and silicon with Au Np (used Eq. 5. 7).

We plotted the resulting absorption coefficient from Eq. 5. 7 in Fig. 5. 8. The result looks slightly different compared to Fig. 5. 6 from Eq. 5. 5 [63]. The Fig. 5. 8 shows the absorption coefficient of bare bulk silicon, silicon with Ag Nps and silicon with Au Nps.

So far we have used only spherical metal Nps, but the same methods can be applied for non-spherical metal Nps as well as for ellipsoids [64].

5.5 J-V Characterisation

After determining the absorption coefficient, we can determine the generation for $electron - hole$ pairs (using Beer's low) given by [24]

$$G(\lambda, x) = \phi(\lambda)\alpha(\lambda)e^{-\alpha(\lambda)x} \tag{5.8}$$

where x is the length of the absorbing material and $\alpha(\lambda)$ is the absorption coefficient of the composite material. Here $\phi(\lambda)$ is the solar photon flux density. Furthermore we assume that all photons pass into the solar cell (no reflection). The enhancement of the photocurrent current density from the

composite solar cell can be calculated using

$$\Delta J_p = -q \int_{\lambda_1}^{\lambda_2} \int_0^L G(\lambda, x) dx \tag{5.9}$$

where q is the elementary charge. We integrated over wavelength from $\lambda_1 = 300\ nm$ to $\lambda_2 = 1100\ nm$. Our calculations showed better performance for silicon with silver spherical Nps as compared to silicon with gold spherical Nps. Fig. 5. 9 shows the current voltage curve of the bare silicon solar cell, and for spherical Ag and Au Nps embedded into a silicon cell. In order to predict the $J - V$ curve the General-purpose Photovoltaic Device Model (GPVDM) simulation program was used [38]. The resulting $J - V$ curve for a thin film c-Si solar cell is given by Fig. 5. 9 and as can calculate from the $J - V$ curve $J_{sc,Si} = 226.26$ open circuit voltage is $V_{oc} = 0.454$ and all necessary parameters were given in table 5. 1.

Parameters	Symbol	Value
Electron mobility $[\frac{m^2}{Vs}]$	μ_n	5×10^7
Hole mobility $[\frac{m^2}{Vs}]$	μ_p	4.5×10^6
Donor doping concentration $[m^{-3}]$	N_D	5×10^{26}
Acceptors doping concentration $[m^{-3}]$	N_A	5×10^{26}
Static relative permittivity	ϵ	11.7
Band gap $[eV]$	E_{gap}	1.6
Temperature $[K]$	T	300

TABLE 5.1: The main input parameters for a thin film c-Si p/n junction solar cell.

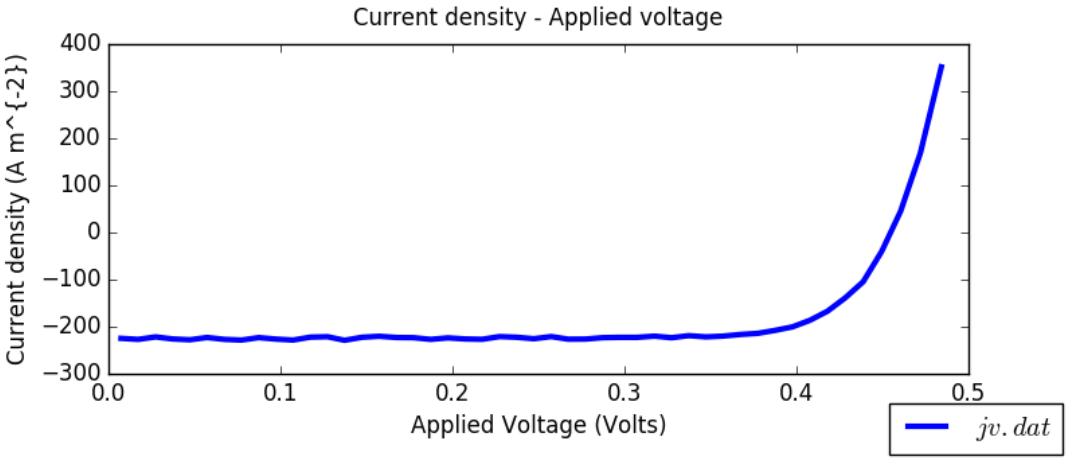


FIGURE 5.9: J-V curve for thin-film c-Si solar cell simulated using GPVDM.

To analyse the performance of a thin-film c-silicon solar cell, the data in table 5. 1 has been used to calculate the efficiency η. The enhancement of short

circuit current density for the $Si-Au$ composition $\Delta J_{sc,Si-Au}$ is 104 Am^{-2} and for $Si-Ag$ composition $\Delta J_{sc,Si-Ag}$ is 44 Am^{-2} To calculate the efficiency, η we will use same method that we used in the previous chapter. It was defined as

$$\eta = \frac{P_{out}}{P_{in}} \times 100\% \tag{5.10}$$

where $P_{in} = 1000W/m^2$ is input solar power density and output power density $P_{out} = J_m \times V_m$.

$J_{m,Si}$	219 Am^{-2}
$J_{m,Si-Au}$	$\sim$ 290 Am^{-2}
$J_{m,Si-Ag}$	$\sim$ 350 Am^{-2}
$V_{m,Si}$	0.37 V
$V_{m,Si-Au}$	$\sim$ 0.37 V
$V_{m,Si-Ag}$	$\sim$ 0.37 V
η_{Si}	8.1 %
η_{Si-Au}	13.6 %
η_{Si-Ag}	11 %

TABLE 5.2: Performance of a thin film c-Si solar cell with and without embedded plasmonic Nps.

In order to calculate the efficiency enhancement from the composite materials, we added up the additional current density due to the plasmonic nanoparticles to the J_{sc} of solar cell without plasmonic nanoparticles to approximate $V_{m,Si-Au}$, $V_{m,Si-Ag}$, $J_{m,Si-Au}$ and $J_{m,Si-Ag}$. The calculation results given by table 5. 1. We predict 2.9 per cent enhancement from $Si-Ag$ and 5.5 % for $Si-Au$. This is based on calculations using 10 nm Nps which are suitable to show plasmonic effects, the Np size can be optimized in future work.

Chapter 6

Judd-Ofelt Theory

6.1 Introduction

As we discussed in the previous chapter, the losses in efficiency of a single-junction solar cell was over 40 per cent because of thermalisation and transmission [65]. Here we will discuss methods to reduce these losses, using frequency conversion techniques based on rare earth ions. To this end a solar cell will be augmented by extra layers of glass which are doped with rare-earth (RE) ions. These extra layers are placed on the top and back of solar cells. In the following section we will give some background information about glass layers containing RE ions.

6.1.1 Glasses

Due to the high transparency of glass for visible light it is very commonly used in daily life and technology like optical instruments, windows and photonic devices [65, 66]. Moreover, its fabrication is easy and cheap. The sol-gel technology can be used for the fabrication of quality glass and it is often the experimental method of choice to implement frequency conversion techniques in solar cells [67]. Note that the glass for frequency conversion applications requires low optical scattering and low ionic/atomic absorption. For more information see ref. [65]

6.1.2 Rare-Earth Ions

In this study, RE ions are used in a composite with glass to enhance the efficiency of solar cells. The RE ions let the cells make better use of light which is outside the visible range. An amazing property of rare-earth (RE) ions is their ability to convert light from near-infrared or UV range into the visible range. Therefore, there are many practical applications in optics based on RE ions [68–70]. Below, we give a short introduction to Judd-Ofelt (JO) theory, which describes characteristics of the transition properties of RE-glass, including important concepts like oscillator strengths, branching ratio, lifetime, intensity parameters and transition probability [71].

6.1.3 Spectroscopy of Rare-Earth Ions

Spectroscopy studies are based on the interaction between light and matter, and it is particularly concerned with how matter will absorb or emit light of different frequencies. The energy of this absorbed or emitted light is related to electrical and structural characteristics of matter.

This way one can also get information about single atoms such as, the valence or excited state of electrons in an atom. It is useful to know how to identify the energy levels of an atom. Atomic states are usually labeled by the symbol ,

$$^{2S+1}L_J,$$

where S is the total spin quantum number, L is the label of the total orbital angular momentum and J is the total angular momentum ($l + s \geq j \geq l - s$) The ground state of an element like Erbium (Er) is influenced by the spin-orbit coupling, the *Pauli exclusion principle* and Hund's rule. These rules tell us how the electrons are distributed in the available orbitals (for more detail about the Hund rules and Pauli exclusion principle see ref. [72]). The electronic configuration of an Er atom for example is [Xe] $6s^2$:$4f^{12}$. Let us apply three Hund rules to determine the corresponding spectroscopic symbol. Here are three Hund rules, respectively

1. Rule To filling the shells

$Er : [Xe]6s^2 : 4f^{12}$	$= \uparrow\downarrow$	$\uparrow\downarrow$	$\uparrow\downarrow$	$\uparrow\downarrow$	$\uparrow\downarrow$	$\uparrow$	$\uparrow$
m_l	$= 3$	2	1	0	-1	-2	-3

2. Rule To sum over spin up and down

$$S = \sum_{i=1}^{7} S_i = 1$$

Total spin is $2S + 1 = 3$ which is triplet level

3. Rule To sum over both spins

$$l = \sum_{i=1}^{7} (m_l)_i = 5$$

which is the H-term in spectroscopic notation. The subshell is more than half filled so the maximum value of J is, $s + l = 5 + 1 = 6$. This is used to specify the ground state electron configuration, then $^{2S+1}L_J = {}^3H_6$ [73].

Following the same method the ground state electron configuration of Er^{3+} ion can be stated as $^4I_{15/2}$.

Selection rules

Optical transitions in RE ions are characterised by the selection rules tabulated in table 6.1 for a free ion and in in the presence of an external electric field. These rules will change for high applied electric and magnetic fields. [71].

Free ion case	External field case
Angular momentum L: Δ L = 0, $\pm$ 1	Forced electric dipole Δl= $\pm$1, ΔL, ΔJ $\leq 2l$, ΔS = 0 for 0 $\leftrightarrow$ 0 transition
Total angular momentum J: ΔJ = 0, $\pm$ 1	Forced magnetic dipole ΔL = 0, ΔJ = 0, $\pm$ 1, ΔS= 0
Spin quantum number S: ΔS= 0	Quadrupole ΔJ= 0, $\leq \pm 2$
Magnetic dipole transition M: ΔL = 0, $\pm$ 1, $\pm$ 2, ΔJ = 0, and ΔS = 0	

TABLE 6.1: Selection rules for various types of transition in rear-earth ions [74].

The quantum numbers L, J, S and M describe the state of electrons a material.

6.2 Analysis of Jodd- Ofelt Theory

Jodd-Ofelt (JO) theory analysis describes the intensities of f-f transitions in the spectra of lanthanide compounds [71].

Before we go into the details let us describe some of the properties of RE. There are two types of rare-earth ions; the first type is divalent with electronic, $4f^N 5s^2 5p^6$, configuration, and the second type is trivalent with $4f^{N-1} 5s^2 5p^6$ electronic configuration. Some typical divalent rare earth ions are Europium (Eu^{2+}), Ytterbium (Yb^{2+}), Samarium (Sm^{2+}) and some trivalent rare earth ions are Thulium (Tm^{3+}), Erbium (Er^{3+}), Praseodymium (Pr^{3+}), Cerium (Ce^{3+}). The electrons in the f shell are shielded by the $5s, p, d$ shell which leads to atomic-like spectroscopy properties of these inner shells . The Fig 6. 1 shows the energy level diagram of RE ions. Because of a weak crystal field effect the energy levels of free ions and in crystal are similar. For a discussion of the corresponding Hamiltonian see [75].

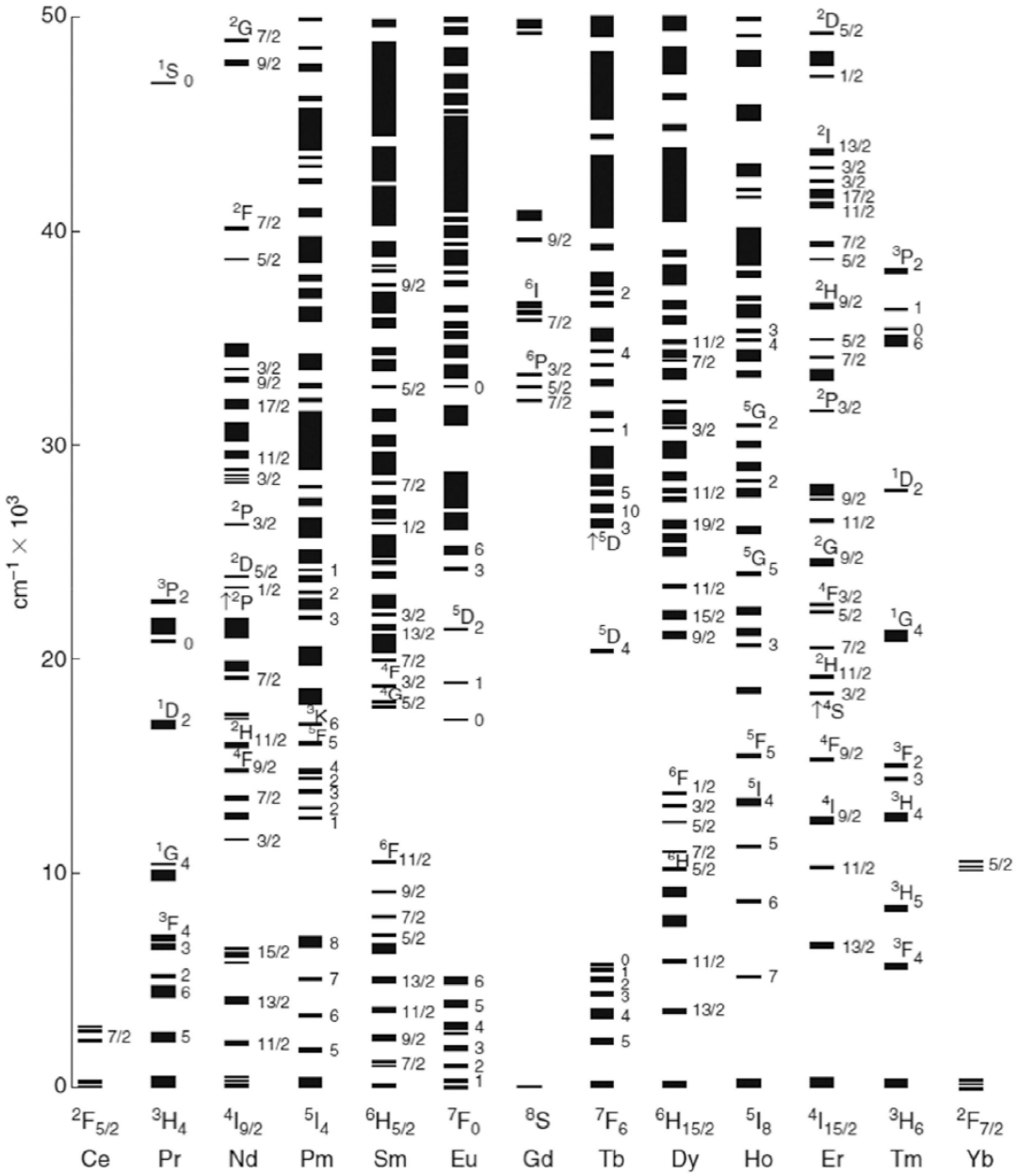


FIGURE 6.1: Energy levels of rare-earth ions in the $4f^n$ configuration. Adopted from ref. [76]

Experimental oscillator strength values (for f-f transitions) for crystals are usually found by integrating the absorption band of a RE doped crystal as [77],

$$f_{exp} = 4,32x10^{-9}(cd)^{-1}\int \sigma(\lambda)d\sigma, \tag{6.1}$$

where c is the concentration of the lanthanide ions in $mole^{-1}$ and d is the optical path length. The oscillator strengths may also be calculated using

$$f_{cal} = \frac{8\pi^2 mc\nu}{3h(2j+1)}\frac{(n^2+2)^2}{9n}\sum_{\lambda=2,4,6}\Omega_\lambda|\langle f^n\psi J||U^{(\lambda)}||f^n\psi' J'\rangle|^2, \tag{6.2}$$

where m is the mass of electron, c is the speed of light in vacuum, h is Plank's constant, n is the refractive index of the surrounding medium, J is the total angular momentum of the initial state ν is the transition energy and Ω_λ is the JO intensity parameters. Transitions between J multiplets are valid for only three JO intensity parameters Ω_2, Ω_4 and Ω_6. The value of these parameters are extracted from experimental results by fitting theoretical oscillator strengths to the experimental data[78]. These Ω_λ parameters help to analyse the relations between spectra and structural properties of lanthanide complexes of different kinds. Note that the matrix elements were tabulated by Carnall *et al.* [79] and JO intensity parameter Ω_2, Ω_4 and Ω_6, are determined by a least squares fit using experimental data[80, 81].

The oscillator strength is calculated based on Eq. 6. 2, and it is proportional to the electric dipole strength S_{ed}

$$S_{ed} = \sum_{\lambda=2,4,6} \Omega_\lambda |\langle f^n \psi J || U^{(\lambda)} || f^n \psi' J' \rangle|^2 \tag{6.3}$$

and the magnetic dipole S_{md} strength

$$S_{md} = \frac{h^2}{16\pi^2 m^2 c^2} |\langle f^n \psi J | L + 2S | f^n \psi' J' \rangle|^2 \tag{6.4}$$

The radiative transition probability is the total matrix element of the electric dipole plus the magnetic dipole transitions $(ED + MD)$ between an initial J and final J state. It is given by,

$$A(J', J) = \frac{64\pi^4 e^2}{3h(2J'+1)\overline{\lambda}^3} \left[n \left(\frac{n^2+2}{3}\right)^2 S_{ED} + n^2 S_{MD} \right] \tag{6.5}$$

Where e is the electron charge (in electrostatic unit) and $\overline{\lambda}$ is the mean wavelength. The radiative lifetime τ_r, and the branching ratio, β [71], can be calculate by the following equations;

$$\frac{1}{\tau_r} = \sum_J A(J'; J) \tag{6.6}$$

$$\beta_{J';J} = \frac{A(J'; J)}{\tau_r} \tag{6.7}$$

These parameters are important when calculating the lifetime of transition processes and the intensity of emission lines that are used for UC and DC conversion as discussed in the following chapter. The emission cross-section $\sigma(\lambda)$ is

$$\sigma_{0,abs}(\lambda) = \frac{\lambda^4}{8\pi c n^2 \Delta\lambda_{eff}} A(J'; J) \tag{6.8}$$

Where $\Delta\lambda_{eff}$ is a line shape function which may be obtained from

$$\Delta\lambda_{eff} = \frac{\int I(\nu)d\nu}{I}. \tag{6.9}$$

Note that $I(\nu)$ is irradiance as a function of frequency ν. A frequency dependent cross-section may be obtained from

$$\sigma(\omega)_{abs} = \sigma_{0,abs}\frac{\Gamma^2/4}{(\omega-\omega_0)^2+\Gamma^2/4} \tag{6.10}$$

Where $\Gamma = A(J';J)$ and $\omega = 2\pi c/\lambda$.

After going through JO theory we can determine the absorption coefficient of RE ions. Here rare earth ion is Dy^{3+} and embedded in transparent materials such as glass-$CaBA$. $CaBA$ that plays a role as a host material. This material is illuminated with 355 nm wavelength by a Nd:YAG laser. The material absorbs the laser light ($\lambda = 355\ nm$) and re-emits three different wavelengths that correspond to 660 nm ($4f_{9/2} \rightarrow 6H_{11/2}$), 575$nm$ ($4f_{9/2} \rightarrow 6H_{13/2}$) and 475$nm$ ($4f_{9/2} \rightarrow 6H_{15/2}$)[82] (see Fig. 6. 3). This is a

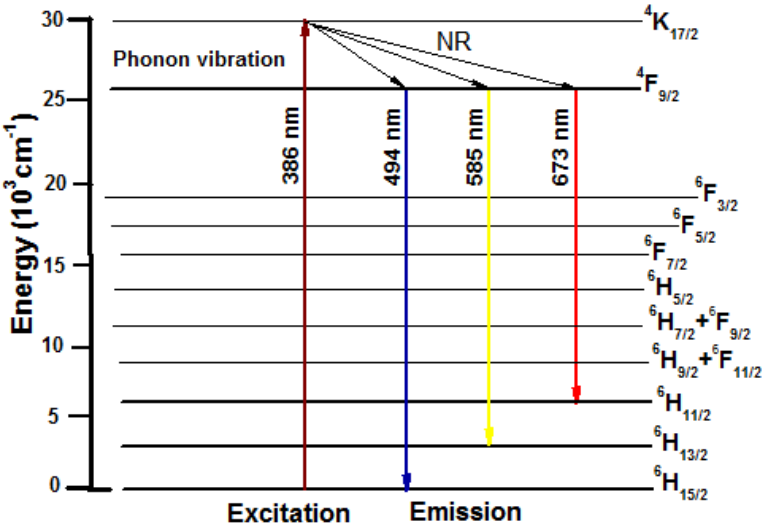


FIGURE 6.2: Energy level diagram for Dy^{+3} in a glass with possible transitions. Adopted from ref. [82]

significant process that converts high energy photons in the UV region to up to three lower energy photons in the visible region. This process is photon downconversion. Such a layer would reduce the thermalisation of electrons which normally increases the temperature of the device and for this reason the efficiency will increase.

Fig. 6. 3 shows the corresponding absorption cross-sections (by Eq. 6. 10), using the parameters given in table. 6. 2. They correspond to

$4F_{15/2} \rightarrow 6H_{11/2}$ (at $673nm$ wavelength), $4F_{15/2} \rightarrow 6H_{13/2}$ (at $585nm$ wavelength) and $4F_{15/2} \rightarrow 6H_{15/2}$ (at $494nm$ wavelength)

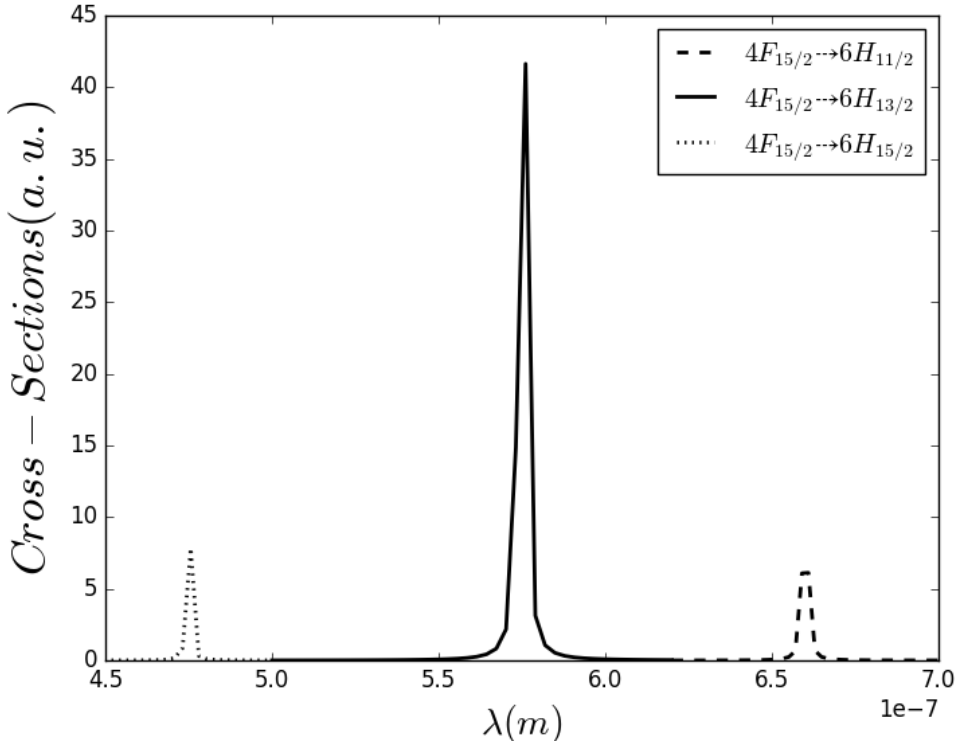


FIGURE 6.3: Emission cross-section of $Dy : CaBA$. where the excitation wavelength is $\lambda = 355\ nm$.

From the relationship between the emission and absorption cross-section that was calculated using the McCumber theory [83], we can determine the emission cross-section $\sigma_{emis}(\omega)$. The relationship is given by

$$\sigma_{emis}(\omega) = \sigma_{abs}(\omega) exp\Big(\frac{\epsilon - h\nu}{k_b T}\Big). \tag{6.11}$$

Where ϵ is the energy for a transition from the ground state to an excite state, ν is the photon frequency of the emitted photon, T is the temperature, h is the Planck constant and k_b is the Boltzmann's constant.

	$4F_{9/2} \rightarrow 6H_{11/2}$	$4F_{9/2} \rightarrow 6H_{13/2}$	$4F_{9/2} \rightarrow 6H_{15/2}$
$\sigma_{0,abs}$	$5.49 \times 10^{-26}\ m^2)$	$37.2 \times 10^{-26}\ m^2)$	$5.81 \times 10^{-26}\ m^2)$
A(J';J)	0.089	0.853	0.264
λ_0	660 nm	575 nm	475 nm
n		1.65	

TABLE 6.2: Necessary parameters for plotting absorption cross-section of $Dy : CaBA$ [84].

By a similar technique , we can convert the light from the infrared region to the visible region by a process of up-conversion (UC) see Fig 6. 4. Fig 6. 4 shows the schema of UC. Here using an excitation wavelength 780 nm the following emission wavelengths are observed: 374 nm, 547 nm, 656 nm and 714 nm.

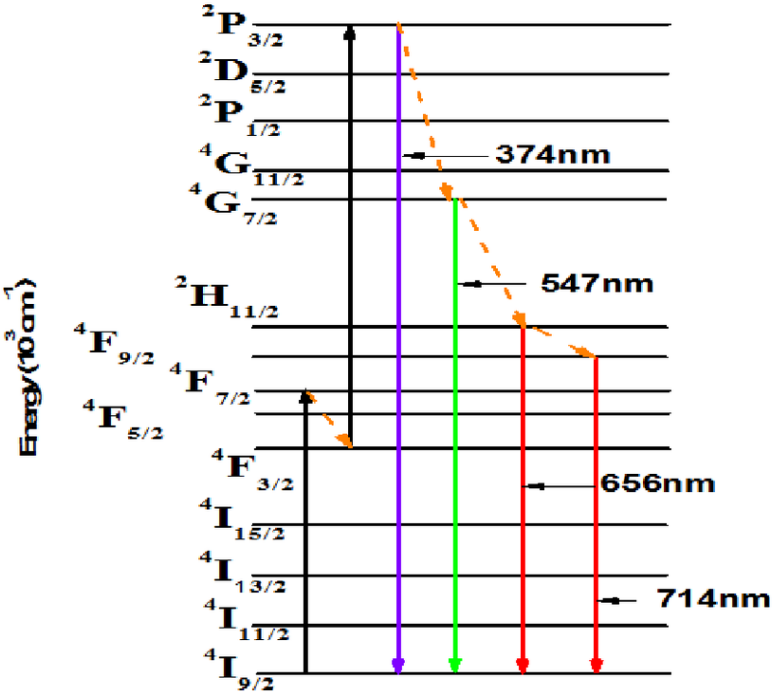


FIGURE 6.4: Energy-level scheme of the Nd^{+3}-doped

In the following chapters, we will discuss two different methods for increasing the efficiency of the solar using UC and DC.

Chapter 7

Up and Down Conversion and Their Application to Solar Cells

7.1 Introduction

In the previous chapter, we discussed plasmonic nanoparticles as a new approach to increase the efficiency of solar cells. Now we will use another approach based on up-conversion (UC) and down-conversion (DC). With UC/DC we basically modify the solar spectrum experienced by the solar cell. Standard conventional solar cells cannot utilise all photons in the solar spectrum. Photons with sub-band-gap energies cannot be absorbed by conventional Si solar cells, and 20 per cent of the solar energy that reaches earth's surface is wasted [16, 85]. Other losses are from photons with excess energy (w.r.t the band gap). They lose their excess energy through thermalisation, causing heating of the solar cell which decreases their efficiencies [86].

In order to prevent losses from photons, with energies largely different from the electronic band gap, we will use UC and DC methods respectively. To supply a solar cell with UC/DC one of the easiest techniques is to implement layers made of a luminescent material such as a glass layer doped withe rare-earth ions which is placed on top (DC) or at the bottom (UC) of a solar cell as a extra layer.

Theoretically, the efficiency of silicon solar cells with DC can be increased up to 38.6 per cent and with both DC and UC one may reach up to 47.6 per cent[11]. In the following sections, we will discuss UC and DC for a couple of rare-earth ions and examine their application in c-Si based solar cells.

7.1.1 Photon absorption and emission theory

Before going into the details of UC and DC processes, it might be useful to recall some well established and relevant interactions and processes, such as ground state absorption (GSA), exited state absorption (ESA) and spontaneous emission (SPE). These processes are sketched in Fig. 7. 1.

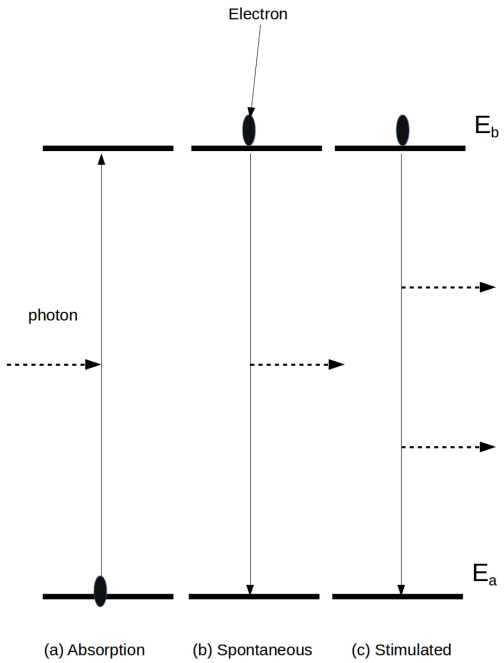


FIGURE 7.1: Absorption and emission process between two energy levels.

To determine the output intensity of a UC system, we can consider a system with an number of incoming photons N_p that all have an energy ΔE_{ab}. The density of atoms in the ground and the excited state are N_a and N_b, and their energies are E_a and E_b, respectively [87]. The energy difference ΔE_{ab} is given by:

$$\Delta E_{ab} = E_b - E_a \tag{7.1}$$

The absorption of photons within this system is proportional to the number of incoming photons with energy ΔE_{ab} . Photons that can be absorbed by the ground state are given by:

$$\left(\frac{dN_p}{dt}\right)_{abs} = -B_{ba}N_bN_p \tag{7.2}$$

where B_{ba} is the Einstein coefficient that depends on the properties of states N_a and N_b.The negative sign indicates that the photon number decreases as the photons are absorbed. The stimulated emission is given by:

$$\left(\frac{dN_p}{dt}\right)_{stim} = B_{ba}N_bN_p \tag{7.3}$$

Finally, the spontaneous emission is not dependent on the incoming photons. It is given by:

$$\left(\frac{dN_p}{dt}\right)_{spon} = AN_b \tag{7.4}$$

A is the Einstein coefficient, which is related to the radiative life time. Under steady state conditions, the total number of photons in the system is given by:

$$\left(\frac{dN_p}{dt}\right)_{abs} + \left(\frac{dN_p}{dt}\right)_{stim} + \left(\frac{dN_p}{dt}\right)_{spon} = 0 \tag{7.5}$$

The ratio of the population density of the upper level N_b and lower level N_a is described by Boltzmann distribution function

$$\frac{N_a}{N_b} = exp\left(\frac{\Delta E}{k_b T}\right) \tag{7.6}$$

Where k_b is Boltzmann constant and T is the prevailing temperature. Solving for N_p, we obtain:

$$N_p = \frac{A}{B_{ba}\left(\frac{N_a}{N_b} - 1\right)} \tag{7.7}$$

The general total emission is given by:

$$\left(\frac{dN_p}{dt}\right)_{tot} = B_{ba}N_b(N_p + 1) \tag{7.8}$$

This theory helps to calculate the flux caused by converted photons. The extra flux Φ over the length d of the material sample is given by:

$$\Phi = \left(\frac{dN_p}{dt}\right)_{tot} d \tag{7.9}$$

7.2 Up and Down Conversion

UC converts two or more photons into a higher energetic photon for harvesting the sub-band-gap photons and adding them to the visible spectrum that may be absorbed by a solar cell and generate extra current [11, 12, 88]. Therefore, UC provides an attractive method of reducing the spectral losses and improving overall efficiency of the solar cells. This enhancement from an UC material can be applied to all kinds of solar cells.

DC is the reverse process of UC, where higher energy photons are converted to lower energy photons [89]. DC is usually driven by ultraviolet photons. About 35 per cent of the solar energy that reaches the earth's surface is lost by thermal effect due to the mismatch with the band-gap of the semiconductor material. The DC layer in solar cells will absorb ultraviolet (higher energy) photons and split them into photons closer to the band gap

energy. The same theory for calculating the current density from UC, can be applied to DC. The ideal QE of DC should be 200 per cent, because one photon is converted to at least two photons.

The UC/DC materials are to be implemented as extra layers. The UC layer should be placed under the solar cell, because low energetic photons can not be absorbed and are transmitted through the solar cell. After UC the higher energetic photons will be reflected at the back contacts and delivered into the active layer of a solar cell. A DC layer should be placed on the top of a solar cell to absorb more high energetic photons and convert them into the visible range before reaching the active layer of the solar cell. Fig. 7. 2 illustrates the structure of solar cell with frequency conversion layers.

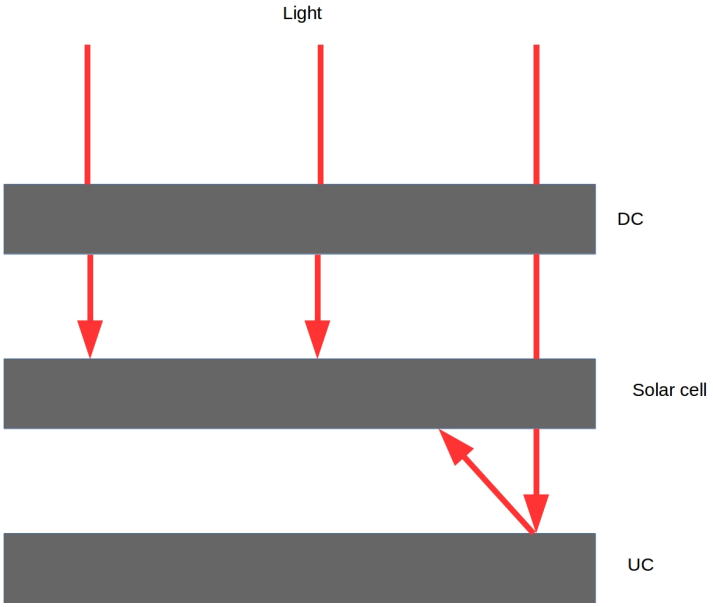


FIGURE 7.2: Schematic view of a solar cell with UC and DC layers.

7.3 Rate Equations for Up/Down-Conversion

7.3.1 Up-Conversion Case

We are going to examine some rare-earth ions contained in co-doped glass layers. Typical rare earth ions are Erbium Er^{+3}, Neodymium Nd^{3+}, Yb^{3+} and Thulium Tm^{3+}. These ions are well-known rare-earth elements with favourable energy levels that allow for photo emission within the visible range of the solar spectrum. The term diagram for a typical example of UC is shown by Fig. 7. 3., which highlights the most important optical processes. There are basically three typical transitions, called ground state absorption (GSA) ($^3H_6 \rightarrow^3 H_5$ transition), first excited state absorption (1 ESA) ($^3H_4 \rightarrow^3 F_6$ transition) and second excited state absorption (2 ESA) ($^3F_4 \rightarrow^1 G_4$ transition), which includes a number of metastable states are shown below.

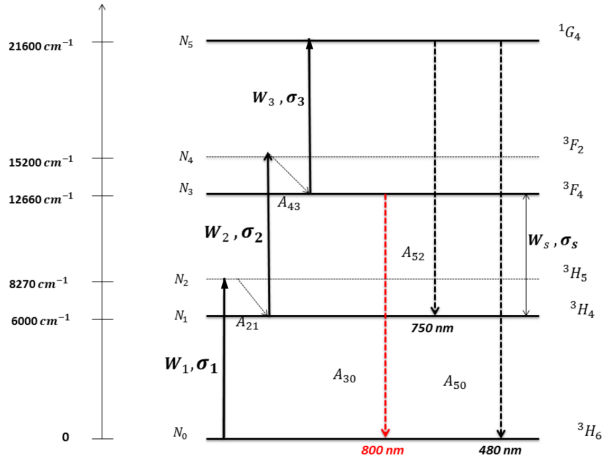


FIGURE 7.3: UC energy level diagram with the most important processes for Tm^{3+} in the fluoride glass [90].

The rate equations for this schema are given by:

$$\begin{aligned}
\frac{dN_0}{dt} &= -W_1N_0 + A_{10}N_1 + A_{30}N_3 + A_{50}N_5 \\
\frac{dN_1}{dt} &= -(A_{10} + W_2 + W_s)N_1 + A_{21}N_2 + W_5N_3 \\
\frac{dN_2}{dt} &= W_1N_0 - A_{21}N_2 + A_{52}N_5 \\
\frac{dN_3}{dt} &= W_sN_1 - (A_{30} + W_s + W_3)N_3 + A_{43}N_1 \\
\frac{dN_4}{dt} &= W_2N_1 - A_{43}N_4 \\
\frac{dN_5}{dt} &= W_3N_3 - (A_{50} + A_{52})N_5 \\
N_{Tm^{+3}} &= N_0 + N_1 + N_3 + N_5
\end{aligned} \tag{7.10}$$

Here W_i is the probability of the pumping transition i, denotes the initial energy level and j, denotes the final level. A_{ij} is the corresponding decay rate. The pumping transition, W_i, is proportional to the pump power ,P_p which is given by:

$$W_i = P_p\sigma_i/E_pA_{eff} \tag{7.11}$$

Where σ_i is the absorption cross-section, E_p is the pump energy and A_{eff} is the effective cross-section. The population density of N_2 and N_4 are usually negligible for such a schema [90]. In the steady state ($dN_i/dt = 0$), the population densities , N_0, N_1, N_3 and N_5 can be derived from the equations as a function of the pump power. Provided that all necessary constants in Eq. 7. 10 are known from experimental results. Note that A_{ij} can be calculated by Judd-Ofelt theory as well. The important parameters needed to solve for the population densities are given in table 7. 1 [90].

Parameter	Symbol	Value
GSA cross section	σ_1	$1.1 \times 10^{-21}\ cm^2$
1 ESA cross section	σ_2	$8.2 \times 10^{-19} cm^2$
2 ESA cross section	σ_3	$1 \times 10^{-20}\ cm^2$
stimulation cross section	σ_s	$6.7 \times 10^{-19}\ cm^2$
Decay rate from the level 1 to 0	A_{10}	$108.6\ s^{-1}$
Decay rate from the level 2 to 0	A_{30}	$594.6\ s^{-1}$
Decay rate from the level 5 to 0	A_{50}	$491.8\ s^{-1}$
Decay rate from the level 5 to 2	A_{52}	$384.4\ s^{-1}$
Total population density	$N_{Tm^{+3}}$	$5 \times 10^{26}\ m^{-3}$
Pump power	P_p	$0.2\ W$

TABLE 7.1: Parameters for solving the rate equations of Eq. 7. 10.

For Tm^{3+} ions in the fluoride glass, we neglect energy transfer between the ions (i.e. assuming that the ions are far enough from each other) we analysed the corresponding up-conversion scheme. Fig. 7. 3 shows infrared input photons of $1064nm$ and up-converted output photons of 480 nm, 750 nm and 800 nm at visible wavelengths. The initial intensity used in the simulation model was the AM1.5 spectral intensity averaged in the UC window to effectively 1064 nm in the infrared range. As we can see from Eqs. 7. 10 and 7. 11 the probability of a transition W_i is proportional to the pump power and the population density of the i state. We will solve the rate equation with a given realistic pump power. To this end Fig. 7. 4 shows the population density as a function of this pump power. Finally we choose here the effective cross-section as $A_{eff} = 0.5 \times 0.5\ \mu m$ for calculate W_i [91].

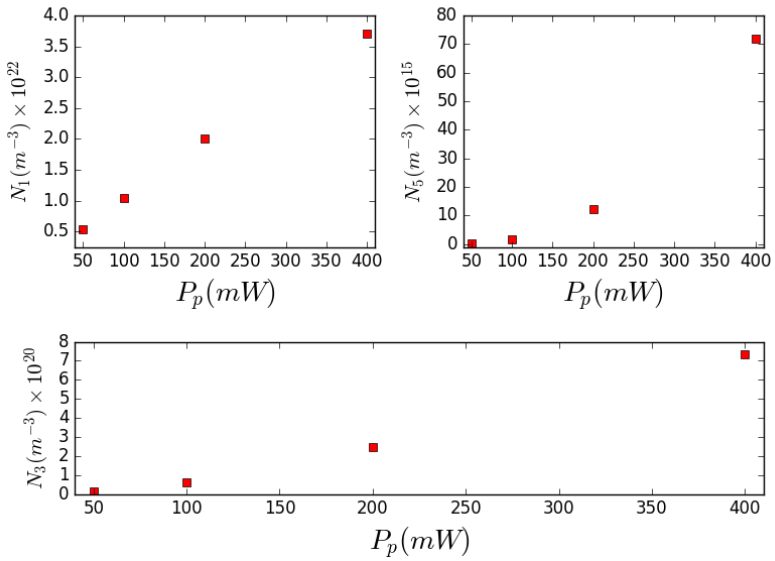


FIGURE 7.4: Population density of state N_1, N_3 and N_5 as a function of pump power for the UC system of Eq. 7. 10.

In Fig. 7. 4, the population densities are proportional to the pump power, and a higher power gives a high population density. But the population density of the ground state N_0 is almost constant and equal to $4.99 \times 10^{26}\ m^{-3}$.

7.3.2 Down-Conversion Case

To illustrate down conversion, we use the system as, Td^{3+}-Yb^{3+} co-doped in fluoroindogallate glass (DC layer). Note that there is an energy transfer (ET) between the two rare-earth ions. With this type of conversion layer, photons can be converted from the ultraviolet range (360 nm) to the near-infrared range (980 nm). The processes of ground state absorption (GSA) and (ET) are shown in Fig. 7.5.

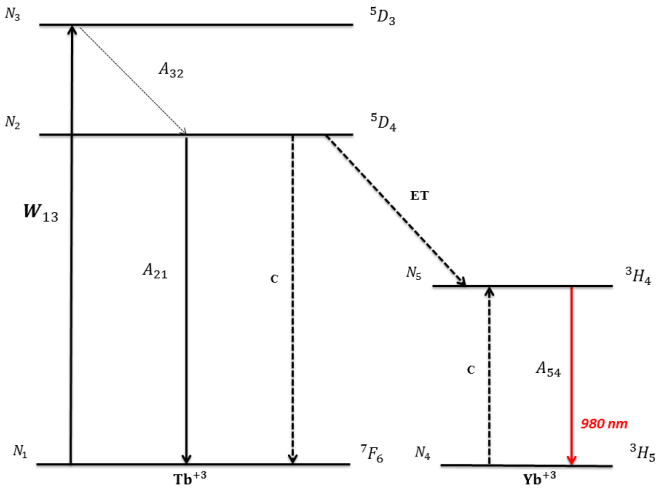


FIGURE 7.5: DC energy level diagram with the important processes for Tb^{3+}-Yb^{3+}.

The rate equation for this schema are given by:

$$\begin{aligned}
\frac{dN_1}{dt} &= -W_{13}N_1 + A_{21}N_2 + CN_2N_4 \\
\frac{dN_2}{dt} &= -A_{21}N_2 - CN_2N_4 - A_{32}N_2 \\
\frac{dN_3}{dt} &= -A_{32}N_3 + W_{13}N_1 \\
\frac{dN_4}{dt} &= A_{54}N_5 - CN_2N_4 \\
\frac{dN_5}{dt} &= CN_2N_4 - A_{54}N_5 \\
N_{TB^{+3}} &= N_1 + N_2 + N_3 \\
N_{Yb^{+3}} &= N_4 + N_5
\end{aligned} \tag{7.12}$$

Again these rate equations are solved under steady state conditions for a given total population density. The parameters for solving the rate equations are summarised in table 7. 2.

Paramiter	Symbol	Value
GSA cross section	σ_{13}	$1.38 \times 10^{-26}\ m^2$
Decay rate from the level 2 to 1	A_{21}	$150.19\ s^{-1}$
Decay rate from the level 3 to 2	A_{32}	$48030\ s^{-1}$
Decay rate from the level 5 to 4	A_{54}	$10\ s^{-1}$
ET coefficient	C	$2 \times 10^{(}-21)\ m^{-3}$
Total population density of Tb^{3+}	$N_{Tb^{3+}}$	$3 \times 10^{25}\ m^{-3}$
Total population density of Yb^{3+}	$N_{Tb^{3+}}$	$3 \times 10^{25}\ m^{-3}$

TABLE 7.2: Parameters for solving the rate equations of DC [92].

Note that C is the ET cross-relaxation coefficient that relates to concentration of the rare-earth ions [13, 93].

Fig.7.5 shows that the input photons have a wavelength of 360 nm and the output photons have a wavelength of 980 nm, corresponding to DC from an ultraviolet wavelength to a near visible wavelength.

With parameters from table 7.1., 7.2., we solve the rate equations we obtained for DC $N_5 = 8.9 \times 10^{21}\ m^{-3}$. The assumed layer thickness, effective cross-section and pump power are $d = 3\ mm$, $A_{eff} = 0.25\ mm^2$ and $P_p = 0.2$ W for DC.

7.4 Simulation of an Ideal c-Si Solar Cell With and Without UP/Down Conversion

The additional photon flux density from UC or DC, $\phi_{edd,UC/DC}$ over the length d of the conversion material can be estimated by

$$\phi_{edd,UC/DC} = A_{ij} N_i d \tag{7.13}$$

Where N_i is the population density of a state i, from which the electrons decay to a lower electronic state j and emit the converted photons and A_{ij} is decay rate from state i to state j. This additional photon flux must be added to the incoming photon flux from the Sun. It will then generate additional charge carriers in the active region of the solar cell. For a single emission line this

additional generation rate is given by

$$G_{add} = \alpha \phi_{add,UC/DC} \tag{7.14}$$

where α is the absorption coefficient of the solar cells at that specific wavelength. The additional current density due to the conversion layer or material can be estimated using

$$J_{add} = qG_{add}L_D \tag{7.15}$$

where q is the charge of the electron and L_D is the estimated width of the depletion layer. The net current density of the of the augmented solar cell is then given by:

$$J_{net} = J_{dark} - J_p - J_{add} \tag{7.16}$$

Here dark current density, J_{dark} and photocurrent density J_p were already mentioned and calculated in the previous chapter. The last term of the equation, J_{add} is the additional current density coming from the conversion material.

The results from UC and DC and their effect on the solar cell performance are summarized in the table 7. 3.

Parameter	**Symbol**
J_p	42.2 Am^{-2}
$J_{add,UC}$	5.76 $mAcm^{-2}$
$J_{add,DC}$	2.14 $mAcm^{-2}$
α at 800 nm and 980 nm	$\approx 1 \times 10^5$ and $\approx 0.5 \times 10^5$ m^{-1}
L_D	10×10^{-6} m

TABLE 7.3: Performance of the c-Si solar cell with the UP/DC conversion layer.

In relation to the results obtained above, it is important to calculate the efficiency of a solar cell augmented by an additional conversion material layer. Fig. 7. 6 shows the J-V curves of the ideal c- Si solar cell with and without such an additional conversion material layer.

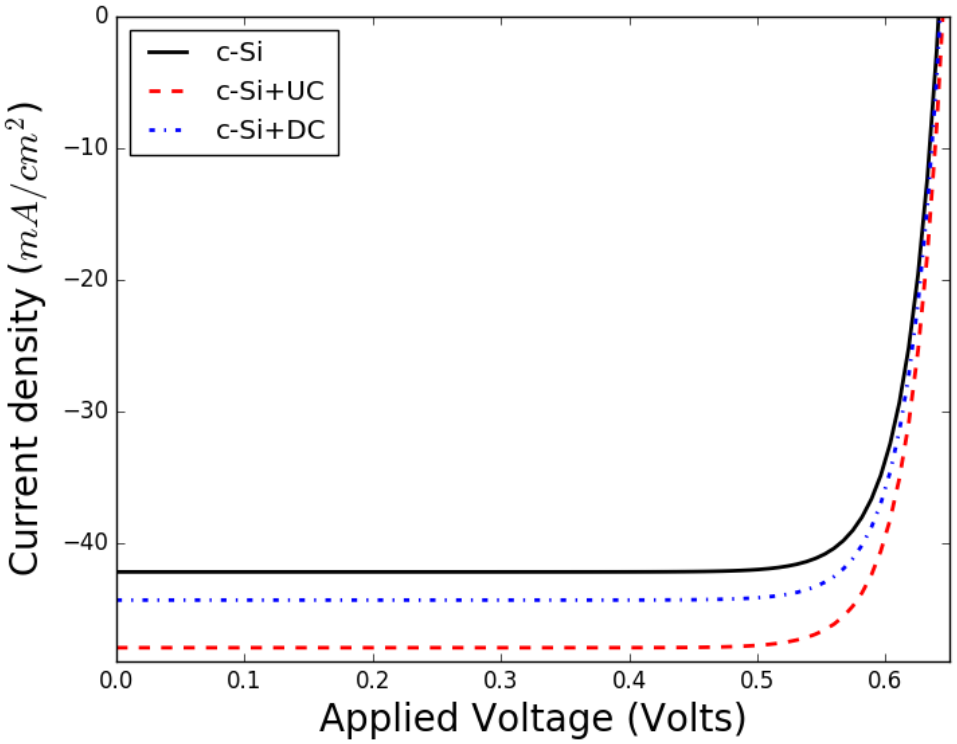


FIGURE 7.6: J-V for ideal c-Si solar cell, and with UC/DC materials.

The percentage of efficiency enhancement $\Delta\eta$ was calculated using the following expression

$$\Delta\eta = \frac{V_{mC} \times J_{mC} - V_m \times J_m}{P_{in}} \cdot 100\% \tag{7.17}$$

Here $P_{in} = 1000\ Wm^{-2}$ is the input solar power, V_m and J_m are the voltage and current density at the maximum power point of the $J-V$ curve, and V_{mC} and J_{mC} are the voltage and the current density at the maximum power point of the of the solar cell augmented by an UC or DC layer, which can be determined from a $J-V$ curve. In the UC case, the infrared photons at our pump wavelength of 1064 nm are utilized by the UC layer and extra photons are produced at the corresponding ($\lambda = 800\ nm$) emission wavelength. For DC ultraviolet photons at a pump wavelength 360 nm are utilised by the DC layer to generate photons at the corresponding (980 nm) emission wavelength. We further assume that each absorbed photon generates one electron-hole pair ($\eta_c = 1$). Then the efficiency enhancement for UC and DC are $\Delta\eta_{UC} \approx 3\%$ and $\Delta\eta_{DC} \approx 2.1\%$.

However note that these efficiencies are strongly dependent on the size of the frequency conversion layers which are fluoride glass for the UC layer and fluoroindogallate glass for DC layer. For our two examples of UC and DC, a different glass layer thickness leads to significant differences in the results (in the percentage range). On the other hand the thicker the glass

layers are, the more UC or DC photons they will absorb and less UC or DC photons will reach the active layer of the solar cell. This absorption may in principle be implemented into the present approach using Beer's law with a suitable absorption coefficient $\alpha(\lambda)$ but for this thesis, we are looking at a method that provides a certain pre-screening of suitable UC and DC schemes, rather than predicting the results of real experiments.

The present approach is only valid for very thin an very transparent glass layer, but it offers a swift method to check the validity and plausibility of experimental results and to suggest new UC and DC system. The goal must be to find a system, which for example offers a 5-10 per cent increase in efficiency for glass layers in the μm range or less.

Chapter 8

Conclusions and Future Work

8.1 Conclusions

We have sketched the physics of a solar cell device and pointed out the limitations of conventional solar cells based on Si. Various processes have been experimentally shown to improve the efficiency of a solar cell like plasmonic nanoparticles and up/down conversion. This would allow efficiencies higher than the Shockley-Queisser limit for a single junction solar cell [9]. In this thesis, we have developed and applied models to implement these new features in a solar cell device simulation, using a simple diode model for c-Si as a starting point. Next, we have focused on strategies to harness light within the infrared and ultraviolet frequency ranges based on UC/DC (up- conversion/down-conversion) processes [8]. We used rare-earth ions and co-doped glass such as Erbium Er^{+3} , Neodymium Nd^{3+} , Yb^{3+} and Thulium Tm^{3+} as an example for UC/DC. Parameters such as the transition lifetimes for the UC and DC processes can be calculated from Judd-Ofelt theory or taken from experimental results. We used rate equations to determine the population density relating to the most promising optical processes in an UC or DC layer. The corresponding photon flux can be used to calculate the extra photo-currents arising from these frequency conversion processes. We showed how to add these photo currents from a single emission line to a generic current model of a typical P-N junction, and estimated the resulting increases in efficiency. The efficiency enhancement of UC and DC was calculated to about 3 per cent and 2.1 per cent respectively but for relatively thick glass layers.

We also noted in our simulation that the rates for the generation of free charges by the incoming sun light are strongly determined by the absorption properties of the basic semiconductor materials used for the p-n junction. These corresponding absorption coefficients may either be taken from experimental or first principles calculations. We also indicated that virtually the whole set of materials parameters necessary to perform device simulations can either be taken from experiment, or they can be also be determined by first principles simulations. We also showed examples of the corresponding device simulations.

We also simulated the absorption and scattering of light using nanoparticles

between $1 - 100\ nm$ diameter which show strong dipolar excitation known as surface plasmon resonances. In particular for thin film solar cells, plasmonic nanoparticles such as Au and Ag can be used to increase the absorption of thin film solar cells. These nanoparticles also scatter light into the active layer of a solar cell, and thus increase the overall efficiency of such as device. We simulated and discussed several scenarios with an up to 5 per cent increase in efficiency, but also presented a model for the heating of a solar cell due to light absorption effects of these nanoparticles, which would reduce the overall efficiency.

This thesis must be seen as part of a worldwide effort to push the efficiency of commercial single-junction solar cells into efficiency ranges, which have only been achieved by expensive complex multi-junction solar cells up to now [85]. Many groups in the world are competing in this field, and new progress is made almost every day. We hope that this thesis will be helpful in this regard, and fill the gap between experimental studies of high efficient solar cells, and typical device simulation of conventional solar cells.

8.2 Future Work

In the future, the methods that were used in this thesis can be applied to both new and established materials such as CdTe and Perovskites. These materials have been studied by many groups worldwide[94]. All the parameters that are needed for the simulation of the corresponding solar cells can be calculated by *ab-initio* methods. Other rare-earth ions and host materials can also be explored in the future, which might be used to develop more efficient frequency conversion schemes in the far infrared or extreme UV range. The Up and Down conversion method can identify new and multiple rare-earth ions to drastically improve solar cell device performance. The methods used for calculating current density related to UC/DC schemes may be related to Beer's law to get more accurate results. We can try different methods to convert photons to energies close the band gap energies to increase the efficiencies of solar cells for example quantum dots. Note that the method that we used for UC/DC was the effect of only one single wavelength photon result. But the solar spectrum has a large range of wavelengths, in the future we may be able to integrate over the UV and IR range of spectrum which can highly increase efficiency in solar cells.

Appendix A

Python Codes for Plotting

A.1 Dielectric Function Based on the Drude-Lorentz Model

```
#Imaginary and Real part of the dielectric function
#for silver and gold using the Drude–Lorentz model
#see Eq. 4. 2 and Fig. 4. 3
import numpy as np
import pylab as pl
from numpy.lib.scimath import logn
from math import e

sol = 3e8 # speed of ligth m/s
tpi = 2 * np.pi
l = np.linspace(250e-9, 1600e-9, 200) # wavelength (m)

#dielectric function for gold
def epsilon_Au(l):
    hb = 6.582119514e-16 # hbar
    w = tpi * sol / l # omega
    epsi = 6.8890 #infinite dielectric constant
    f1 = 1.7857 #Lorentz resonant term
    wp = 8.9601 / hb # plasma frequency
    w1 = 2.9715 / hb # Lorentz resonance frequency
    gamma = 0.0723 / hb #damping term proportional
    gamma1 = 0.9503/hb #Lorentz oscillator damping rate
    return epsi-wp**2/(w**2+1j*gamma*w)-f1*w1**2/(w**2-w1**2+1j*
    gamma1*w)

#dielectric function for silver
def epsilon_Ag(l):
    hb = 6.582119514e-16 # hbar
    w = tpi * sol / l # omega
    wp = 9.2093 / hb # plasma frequency
    w1 = 4.2840 / hb #Lorentz resonance frequency
    gamma = 0.020 / hb #damping term proportional
    gamma1 = 0.3430/hb #Lorentz oscillator damping rate
    f1 = 0.4242 #Lorentz resonant term
    epsi = 3.7180 #infinite dielectric constant
    return epsi-wp**2/(w**2+1j*gamma*w)-f1*w1**2/(w**2-w1**2+ 1j*
    gamma1*w)

epsr = np.real(epsilon_Au(l))
epsi = np.imag(epsilon_Au(l))
```

```
epsgr = np.real(epsilon_Ag(l))
epsgi = np.imag(epsilon_Ag(l))
f, (pl2, pl1) = pl.subplots(1, 2)
pl1.plot(l, epsr, color="black", linewidth=3, linestyle="--", label
    ="Au")
pl1.plot(l, epsgr, color="black", linewidth=3, linestyle="-", label
    ="Ag")
pl2.plot(l, epsi, color="red", linewidth=3, linestyle="--", label="
    Au")
pl2.plot(l, epsgi, color="red", linewidth=3, linestyle="-", label="
    Ag")
pl1.legend(loc='down right')
pl2.legend(loc='upper right')

pl1.ticklabel_format(style='sci', axis='x', scilimits=(1,0))
pl2.ticklabel_format(style='sci', axis='x', scilimits=(1,0))
pl1.set_xlabel(r'$Wavelength(m)$', size=15 )
pl2.set_xlabel(r'$Wavelength(m)$', size=15 )
pl2.set_ylabel(r'$\epsilon_{Drude-Lorentz}$', size=20)
pl1.set_title(r'Re($\epsilon$)', fontsize=20)
pl2.set_title(r'Im($\epsilon$)', fontsize=20)
pl.show()
```

LISTING A.1: Python example

A.2 Scattering and Absorption by Metal Nanoparticles

```
#Scattering and absorption cross-section for Au and
#Ag Nps as a function of the wavelength, and for various radius
#of the metallic nanoparticles. see Eqs. 4. 3, 4. 4 and Fig. 4.5

import numpy as np
import pylab as pl
from numpy.lib.scimath import logn
from math import e

sol = 3e8 # speed of ligth m/s
tpi = 2 * np.pi

l1 = np.linspace(400e-9, 900e-9, 300) # wavelength (m)
l2 = np.linspace(262e-9, 600e-9, 300)

#dielectric function for gold
def epsilon_Au(l):
    hb = 6.582119514e-16 # hbar
    w = tpi * sol / l # omega
    epsi = 6.8890 #infinite dielectric constant
    f1 = 1.7857 #Lorentz resonant term
    wp = 8.9601 / hb # plasma frequency
    w1 = 2.9715 / hb # Lorentz resonance frequency
    gamma = 0.0723 / hb #damping term proportional
    gamma1 = 0.9503/hb #Lorentz oscillator damping rate
    return epsi-wp**2/(w**2+1j*gamma*w)-f1*w1**2/(w**2-w1**2+1j*
    gamma1*w)

```

```
#dielectric function for silver
def epsilon_Ag(l):
    hb = 6.582119514e-16 # hbar
    w = tpi * sol / l # omega
    wp = 9.2093 / hb # plasma frequency
    w1 = 4.2840 / hb #Lorentz resonance frequency
    gamma = 0.020 / hb #damping term proportional
    gamma1 = 0.3430/hb #Lorentz oscillator damping rate
    f1 = 0.4242 #Lorentz resonant term
    epsi = 3.7180 #infinite dielectric constant
    return epsi-wp**2/(w**2+1j*gamma*w)-f1*w1**2/(w**2-w1**2+ 1j*
    gamma1*w)

# polarizability
def alpha_Au(l):
    eps0 = 1
    epsm = 1.8 #dielectric constant of surrounding medium
    Rnp = 80e-9 #radius of the nanoparticles
    eps = epsilon_Au(l)
    return 4*np.pi*eps0*Rnp**3*(eps - epsm)/(epsm + eps)
# polarizability
def alpha_Ag(l):
    eps0 = 1
    epsm = 1.8 #dielectric constant of surrounding medium
    Rnp = 40e-9 #radius of the nanoparticles
    eps = epsilon_Ag(l)
    return 4*np.pi*eps0*Rnp**3*(eps - epsm)/(epsm + eps)

# m**2, Absorption cross-section Au
def abs_Au(l1):
    k = tpi / l1 #wavevector in the medium
    o1 = alpha_Au(l1)
    eps0 = 1
    return k * np.imag(o1)/eps0

# m**2, scattering cross-section Au
def sct_Au(l1):
    k = tpi / l1 #wavevector in the medium
    o1 = alpha_Au(l1)
    eps0 = 1
    return k**4*(np.abs(o1))**2/(6*np.pi*eps0**2)

# m**2, Absorption cross-section  Ag
def abs_Ag(l2):
    k = tpi / l2 #wavevector in the medium
    o1 = alpha_Ag(l2)
    eps0 = 1
    return k * np.imag(o1)/eps0

# m**2, scattering cross-section Ag
def sct_Ag(l1):
    k = tpi / l1 #wavevector in the medium
    o1 = alpha_Ag(l1)
    eps0 = 1
    return k**4*(np.abs(o1))**2/(6*np.pi*eps0**2)

aau = abs_Au(l1)
```

```
sau = sct_Au(l1)
aag = abs_Ag(l2)
sag = sct_Ag(l2)
f, (pl2, pl1) = pl.subplots(1, 2)
pl1.plot(l1, aau, color="red", linewidth=3, linestyle="-", label="
    abs")
pl1.plot(l1, sau, color="black", linewidth=3, linestyle="--", label
    ="scatt")
pl2.plot(l2, aag, color="red", linewidth=3, linestyle="-", label="
    abs")
pl2.plot(l2, sag, color="black", linewidth=3, linestyle="--", label
    ="scatt")
pl1.legend(loc='down right')
pl2.legend(loc='upper right')
pl2.ticklabel_format(style='sci', axis='x', scilimits=(1,0))
pl2.ticklabel_format(style='sci', axis='y', scilimits=(1,0))
pl1.ticklabel_format(style='sci', axis='x', scilimits=(1,0))
pl1.ticklabel_format(style='sci', axis='y', scilimits=(1,0))
pl1.set_xlabel(r'$Wavelength(m)$', size=15 )
pl2.set_ylabel(r'$\sigma (m^2)$', size=20)
pl2.set_xlabel(r'$Wavelength(m)$', size=15 )
pl1.set_title(r'Au $r=80nm$', fontsize=20)
pl2.set_title(r'Ag $r=40nm$', fontsize=20)
pl.show()
```

LISTING A.2: Python example

A.3 Heat Generated by Metal Nanoparticles

```
#Temperature map based Au nanoparticles
#see Eq. 4.12 and Fig. 4. 11
from mpl_toolkits.mplot3d import axes3d
from matplotlib import cm
from matplotlib.ticker import LinearLocator, FormatStrFormatter
import matplotlib.pyplot as plt
import numpy as np
import matplotlib as mpl
sol = 3e8 #m/s, light speed
k0 = 0.6# w/mK, k0 is thermal conductivity
I0 = 1e8 #w/m**2, I0 = c * E_0**2 * eps0**0.5 / 8 * pi, light
    intensity
hb = 6.582119514e-16 # hbar
w = 2*np.pi * sol / 520e-9 # omega
epsi = 6.8890 #infinite dielectric constant
f1 = 1.7857 #Lorentz resonant term
wp = 8.9601 / hb # plasma frequency
w1 = 2.9715 / hb # Lorentz resonance frequency
gamma = 0.0723 / hb #damping term proportional
gamma1 = 0.9503/hb #Lorentz oscillator damping rate

ndim = 50
# total number of NPs in complex
N  = 12
#K, initial temperature
T0 = 271
eps0=1.8
E0=np.sqrt(8*np.pi*I0/(sol*np.sqrt(eps0)))
```

```
#(spherical gold particle radius) m
Rnp = np.array([20e-9,20e-9,20e-9,20e-9,20e-9,20e-9,20e-9,20e-9,20e-9,20e-9, 20e-9])
V_Np = 4*np.pi*Rnp**2/3
epsilon_Au = epsi-wp**2/(w**2+1j*gamma*w)-f1*w1**2/(w**2-w1**2+1j*gamma1*w)
#Q is absorbed power
Q = w*(np.abs(3*eps0/(2*eps0+epsilon_Au)))**2*np.imag(epsilon_Au)*E0**2/(8*np.pi)
#temperature distribution
dT = V_Np*Q / (4 * np.pi * k0)

X = np.linspace(-300e-9, 300e-9, ndim)
Y = np.linspace(-300e-9, 300e-9, ndim)

X, Y = np.meshgrid(X, Y)

X0 = np.array([[50e-9],[150e-9],[50e-9],[150e-9],[-50e-9],[-150e-9],[-50e-9],[-150e-9],[-50e-9],[-150e-9],[50e-9],[150e-9]])
Y0 = np.array([[0],[0],[100e-9],[100e-9],[0],[0],[100e-9],[100e-9],[-100e-9],[-100e-9],[-100e-9],[-100e-9]])

T = np.zeros((ndim, ndim))
#T += T0

for i in range(N):
      T += dT[i] * Rnp[i] / np.sqrt(np.abs(((X - X0[i])**2.0 + (Y - Y0[i])**2.0)))


fig = plt.figure()
ax = fig.add_subplot(111, projection='3d')
ax = plt.gca()


surf = ax.plot_surface(X, Y, T, cmap=plt.cm.coolwarm, rstride=1, cstride=1,linewidth=0, antialiased=False)
ax.view_init(45, -45)

Tmax = np.max(T)

mpl.rcParams.update({'font.size': 16})
ax.zaxis.set_major_locator(LinearLocator(1))
ax.zaxis.set_major_formatter(FormatStrFormatter('%.0f'))

fig.colorbar(surf, shrink = 0.5, aspect=10)
ax.set_xlabel(r'$X(m)$',size=20)
ax.set_ylabel(r'$Y(m)$',size=20)
ax.set_zlabel(r'$\Delta T(K)$',size=20)
plt.show()
plt.clf
```

LISTING A.3: Python example

Appendix B

Publications And Conferences/Workshops Attended

B.1 Publications

⋆ T. Aslan, I. Mokgosi, R. Warmbier and A. Quandt, Solar cell device simulations, Transparent Optical Networks (ICTON). IEEE Xplore, Spain, 2017.

⋆ T. Aslan, I. Mokgosi, R. Warmbier and A. Quandt, Advanced light harnessing features in solar cell device simulations, Transparent Optical Networks (ICTON). IEEE Xplore, Spain, 2018. (Submitted)

⋆ T. Aslan, I. Mokgosi, R. Warmbier, A. Quandt, M. Ferrari and G.Righini, About the implementation of up -conversion processes in solar cell simulations, Glassy Materials Based Microdevices. MDPI, Switzerland, 2018. (submitted)

B.2 Conferences/workshops Attended

⋆ PLESC international workshop, Plasmonics and nanoantennas for solar cells, held on 09/05/2017 at University of the Witwatersrand, Johannesburg/South Africa.

⋆ MERG annual workshop, held on 01/11/2017-02/11/2017 at Societa Dante Alighieri, Johannesburg/South Africa.

⋆ Programme MERG workshop and SA-Italy bilateral project, held on 9.9.2015 at Sunwa River Lodge, Parys/Free State/South Africa.

Bibliography

1. Zhou, B., Pun, E. Y.-B., Lin, H., Yang, D. & Huang, L. Judd–Ofelt analysis, frequency upconversion, and infrared photoluminescence of Ho 3+-doped and Ho 3+/Yb 3+-codoped lead bismuth gallate oxide glasses. *Journal of Applied Physics* **106,** 103105 (2009).
2. Fonash, S. *Solar cell device physics* (Elsevier, 2012).
3. Zernike, F. & Midwinter, J. E. *Applied nonlinear optics* (Courier Corporation, 2006).
4. Pollnau, M., Gamelin, D. R., Lüthi, S., Güdel, H. & Hehlen, M. Power dependence of upconversion luminescence in lanthanide and transition-metal-ion systems. *Physical Review B* **61,** 3337 (2000).
5. Panwar, N., Kaushik, S. & Kothari, S. Role of renewable energy sources in environmental protection: a review. *Renewable and Sustainable Energy Reviews* **15,** 1513–1524 (2011).
6. Fischer, S. Upconversion of sub-band-gap photons for silicon solar cells (2014).
7. Marti, A. & Araújo, G. L. Limiting efficiencies for photovoltaic energy conversion in multigap systems. *Solar Energy Materials and Solar Cells* **43,** 203–222 (1996).
8. Asim, N. *et al.* A review on the role of materials science in solar cells. *Renewable and Sustainable Energy Reviews* **16,** 5834–5847 (2012).
9. Shockley, W. & Queisser, H. J. Detailed balance limit of efficiency of p-n junction solar cells. *Journal of applied physics* **32,** 510–519 (1961).
10. Würfel, P & Würfel, U. *The physics of solar cells: from basic principles to advanced concepts, 2nd updated and expanded ed* 2009.
11. Trupke, T., Green, M. & Würfel, P. Improving solar cell efficiencies by up-conversion of sub-band-gap light. *Journal of Applied Physics* **92,** 4117–4122 (2002).
12. Yang, W., Li, X., Chi, D., Zhang, H. & Liu, X. Lanthanide-doped upconversion materials: emerging applications for photovoltaics and photocatalysis. *Nanotechnology* **25,** 482001 (2014).
13. Song, P. & Jiang, C. Modeling of wavelength downconversion based on the Nd3+–Yb3+ system for improving c-Si solar cell performance. *Journal of Optics* **15,** 025002 (2012).
14. Bansal, A., Sekhon, J. S. & Verma, S. Scattering efficiency and LSPR tunability of bimetallic Ag, Au, and Cu nanoparticles. *Plasmonics* **9,** 143–150 (2014).

15. Atwater, H. A. & Polman, A. Plasmonics for improved photovoltaic devices. *Nature materials* **9,** 205 (2010).

16. Van Sark, W. G., de Wild, J., Rath, J. K., Meijerink, A. & Schropp, R. E. Upconversion in solar cells. *Nanoscale research letters* **8,** 81 (2013).

17. Smith, W. *The action of light on selenium* (British Library, 1876).

18. Cox, B. & Parry, C. Principle. *Smith Junior High School, Mesa AZ* **480,** 4650 (1968).

19. Lashkaryov, V. E. Investigations of a barrier layer by the thermoprobe method. *Izv Akad Nauk SSSR Ser Fiz* **5,** 442–446 (1941).

20. Chodos, A. Bell Labs Demonstrates the First Practical Silicon Solar Cell. *APS Physics* (2009).

21. Tsokos, K. *Physics for the IB Diploma Full Colour* (Cambridge University Press, 2010).

22. Anspaugh, B. E. GaAs solar cell radiation handbook (1996).

23. Nelson, J. *The physics of solar cells* (World Scientific Publishing Company, 2003).

24. Smets, A. H., Isabella, O, Zeman, M, *et al. Solar energy: the physics and engineering of photovoltaic conversion technologies and systems* (UIT, 2016).

25. Gutierrez-Mazzotti, C. UCSB Science Line. *Materials Research Laboratory,(Online). Available:< http://scienceline. ucsb. edu/getkey. php* (2015).

26. Cardona, M. & Pollak, F. H. Energy-band structure of germanium and silicon: The k· p method. *Physical Review* **142,** 530 (1966).

27. Cheung, S. & Cheung, N. Extraction of Schottky diode parameters from forward current-voltage characteristics. *Applied Physics Letters* **49,** 85–87 (1986).

28. May, G. S., Sze, S. M., *et al. Fundamentals of semiconductor fabrication* (Wiley New York, 2004).

29. Fox, M. *Optical properties of solids. Oxford master series in condensed matter physics* 2001.

30. Devices-Part, P. 3: Measurement Principles for Terrestrial Photovoltaic (PV) Solar Devices With Reference Spectral Irradiance Data. *International Organization for Standardization, ISO Central Secretariat, Geneva, Switzerland, ISO/IEC,* 60904–3 (2008).

31. El Faituri, F. Y. & Darkwi, A. *Computer simulation for current density in pn-silicon solar cells* in *Solar Physics and Solar Eclipses (SPSE 2006)* (2006), 163–171.

32. Sze, S. M. & Ng, K. K. Physics of semiconductor devices, ed. *John Willey & Sons,* (1981).

33. Marini, A., Hogan, C., Grüning, M. & Varsano, D. Yambo: an ab initio tool for excited state calculations. *Computer Physics Communications* **180,** 1392–1403 (2009).

34. Quandt, A., Warmbier, R., Mokgosi, I. & Aslan, T. *Solar cell device simulations* in *Transparent Optical Networks (ICTON), 2017 19th International Conference on* (2017), 1–5.
35. Neamen, D. A. *et al. Semiconductor physics and devices* (McGraw-Hill New York, 1997).
36. Onida, G., Reining, L. & Rubio, A. Electronic excitations: density-functional versus many-body Green's-function approaches. *Reviews of Modern Physics* **74,** 601 (2002).
37. Bethe, H. A. & Salpeter, E. E. *Quantum mechanics of one-and two-electron atoms* (Springer Science & Business Media, 2012).
38. MacKenzie, R. C., Kirchartz, T., Dibb, G. F. & Nelson, J. Modeling nongeminate recombination in P3HT: PCBM solar cells. *The Journal of Physical Chemistry C* **115,** 9806–9813 (2011).
39. Green, M. A. Solar cells: operating principles, technology, and system applications (1982).
40. Thoreson, M. D. *et al.* Studies on metal-dielectric plasmonic structures. *Sandia Report SAND2009-7034, Sandia National Laboratories, United States* **41,** 1–68 (2010).
41. Novotny, L. & Hecht, B. *Principles of nano-optics* (Cambridge university press, 2012).
42. Rivera, V., Ferri, F. & Marega Jr, E. in *Plasmonics-Principles and Applications* (InTech, 2012).
43. Polyanskiy, M. N. Refractive index database (2014).
44. Kawabata, A. Electronic properties of fine metallic particles. III. ESR absorption line shape. *Journal of the physical Society of Japan* **29,** 902–911 (1970).
45. Mohammed, F., Warmbier, R. & Quandt, A. in *Recent Trends in Computational Photonics* 341–368 (Springer, 2017).
46. Mie, G. G. Mie, Ann. Phys.(Leipzig) 25, 377 (1908). *Ann. Phys.(Leipzig)* **25,** 377 (1908).
47. Kreibig, U. & Vollmer, M. *Optical properties of metal clusters* (Springer Science & Business Media, 2013).
48. Bohren, C. F. & Huffman, D. R. *Absorption and scattering of light by small particles* (John Wiley & Sons, 2008).
49. Tanner, D. B. Optical effects in solids. *Department of Physics, University of Florida, USA* (2013).
50. Govorov, A. O. *et al.* Gold nanoparticle ensembles as heaters and actuators: melting and collective plasmon resonances. *Nanoscale Research Letters* **1,** 84 (2006).
51. Govorov, A. O. & Richardson, H. H. Generating heat with metal nanoparticles. *Nano today* **2,** 30–38 (2007).

52. Bai, Y. *et al.* Enhancing the Photocurrent of Top-Cell by Ellipsoidal Silver Nanoparticles: Towards Current-Matched GaInP/GaInAs/Ge Triple-Junction Solar Cells. *Nanomaterials* **6,** 98 (2016).

53. Muskens, O., Christofilos, D., Del Fatti, N. & Vallée, F. Optical response of a single noble metal nanoparticle. *Journal of Optics A: Pure and Applied Optics* **8,** S264 (2006).

54. Dykman, L. & Khlebtsov, N. Gold nanoparticles in biology and medicine: recent advances and prospects. *Acta Naturae* **3** (2011).

55. Enrichi, F., Quandt, A. & Righini, G. C. Plasmonic enhanced solar cells: Summary of possible strategies and recent results. *Renewable and Sustainable Energy Reviews* (2017).

56. Ye, F., Burns, M. J. & Naughton, M. J. *Embedded metallic nanopatterns for enhanced optical absorption* in *Next Generation (Nano) Photonic and Cell Technologies for Solar Energy Conversion II* **8111** (2011), 811103.

57. Piralaee, M. & Asgari, A. Modeling of optimum light absorption in random plasmonic solar cell using effective medium theory. *Optical Materials* **62,** 399–402 (2016).

58. Sancho-Parramon, J., Janicki, V. & Zorc, H. On the dielectric function tuning of random metal-dielectric nanocomposites for metamaterial applications. *Optics express* **18,** 26915–26928 (2010).

59. Arefinia, Z. & Asgari, A. An analytical model for optimizing the performance of graphene based silicon Schottky barrier solar cells. *Materials Science in Semiconductor Processing* **35,** 181–188 (2015).

60. Aspnes, D. E. & Studna, A. A. Dielectric functions and optical parameters of si, ge, gap, gaas, gasb, inp, inas, and insb from 1.5 to 6.0 ev. *Physical review B* **27,** 985 (1983).

61. Boroumand Azad, J. Light Trapping in Thin Film Crystalline Silicon Solar Cells (2017).

62. García, M. A. Surface plasmons in metallic nanoparticles: fundamentals and applications. *Journal of Physics D: Applied Physics* **44,** 283001 (2011).

63. Zhao, H. *Light Trapping for Silicon Solar Cells: Theory and Experiment* PhD thesis (Syracuse University, 2013).

64. Tanabe, K. A Simple Optical Model Well Explains Plasmonic-Nanoparticle-Enhanced Spectral Photocurrent in Optically Thin Solar Cells. *Nanoscale research letters* **11,** 236 (2016).

65. Quandt, A., Ferrari, M. & Righini, G. C. in *Sol-gel Based Nanoceramic Materials: Preparation, Properties and Applications* 133–155 (Springer, 2017).

66. Tong, X. C. *Advanced materials for integrated optical waveguides* (Springer, 2016).

67. Najafi, S. I. *Selected papers on sol-gel for photonics* (Society of Photo Optical, 1998).

68. Kumar, R., Nyk, M., Ohulchanskyy, T. Y., Flask, C. A. & Prasad, P. N. Combined optical and MR bioimaging using rare earth ion doped NaYF4 nanocrystals. *Advanced Functional Materials* **19,** 853–859 (2009).
69. Wang, H.-Q., Batentschuk, M., Osvet, A., Pinna, L. & Brabec, C. J. Rare-Earth Ion Doped Up-Conversion Materials for Photovoltaic Applications. *Advanced Materials* **23,** 2675–2680 (2011).
70. DiMaio, J. R., Kokuoz, B. & Ballato, J. White light emissions through down-conversion of rare-earth doped LaF 3 nanoparticles. *Optics express* **14,** 11412–11417 (2006).
71. Walsh, B. M., Barnes, N. P. & Di Bartolo, B. Branching ratios, cross sections, and radiative lifetimes of rare earth ions in solids: Application to Tm 3+ and Ho 3+ ions in LiYF 4. *Journal of applied physics* **83,** 2772–2787 (1998).
72. Xu, R. & Dai, Z. Alternative mathematical technique to determine LS spectral terms. *Journal of Physics B: Atomic, Molecular and Optical Physics* **39,** 3221 (2006).
73. Aygün, E. & Zengin, M. *Atom ve molekül fiziği* (Bilim Yayınları, 1998).
74. Walsh, B. M. in *Advances in Spectroscopy for Lasers and Sensing* 403–433 (Springer, 2006).
75. Biju, P. R. Fluorescence kinetics and energy transfer mechanism in rare earth doped glasey matrices (1998).
76. Shionoya, S., Yen, W. M. & Yamamoto, H. *Phosphor handbook* (CRC press, 2006).
77. Mondry, A. & Bukietyńska, K. The power and limits of the JuddâĂŤOfelt theory: a case of Pr3+ and Tm3+ acetates and dipicolinates. *Molecular Physics* **101,** 923–934 (2003).
78. Tanabe, S., Ohyagi, T., Soga, N. & Hanada, T. Compositional dependence of Judd-Ofelt parameters of Er 3+ ions in alkali-metal borate glasses. *Physical Review B* **46,** 3305 (1992).
79. Carnall, W. T., Fields, P. R. & Rajnak, K. Spectral intensities of the trivalent lanthanides and actinides in solution. II. Pm3+, Sm3+, Eu3+, Gd3+, Tb3+, Dy3+, and Ho3+. *The Journal of Chemical Physics* **49,** 4412–4423 (1968).
80. Judd, B. R. Optical absorption intensities of rare-earth ions. *Physical review* **127,** 750 (1962).
81. Ofelt, G. S. Intensities of crystal spectra of rare-earth ions. *The Journal of Chemical Physics* **37,** 511–520 (1962).
82. Bulus, I., Dalhatu, S. A., Isah, M., Hussin, R. & Soje, E. A. STRUCTURAL AND LUMINESCENCE CHARACTERIZATION OF LITHIUM-BOROSULFOPHOSPHATE GLASSES CONTAINING DYSPROSIUM IONS. *Science World Journal* **12,** 98–101 (2017).
83. Rolli, R. *et al.* Erbium-doped tellurite glasses with high quantum efficiency and broadband stimulated emission cross section at 1.5 μm. *Optical materials* **21,** 743–748 (2003).

84. Van Do, P. *et al.* Optical properties and Judd–Ofelt parameters of Dy3+ doped K2GdF5 single crystal. *Optical Materials* **35,** 1636–1641 (2013).

85. Polman, A. & Atwater, H. A. Photonic design principles for ultrahigh-efficiency photovoltaics. *Nature materials* **11,** 174 (2012).

86. Verma, D., Saetre, T. O. & Midtgård, O.-M. *Review on up/down conversion materials for solar cell application* in *Photovoltaic Specialists Conference (PVSC), 2012 38th IEEE* (2012), 002608–002613.

87. Wayne, R. A Reinterpretation of Stimulated Emission as Spontaneous Emission Under Non Thermodynamic Equilibrium Conditions. *AFRICAN REVIEW OF PHYSICS* **11,** 17–22 (2016).

88. Fischer, S. *et al.* Enhancement of silicon solar cell efficiency by upconversion: Optical and electrical characterization. *Journal of applied physics* **108,** 044912 (2010).

89. Lian, H. *et al.* Rare earth ions doped phosphors for improving efficiencies of solar cells. *Energy* **57,** 270–283 (2013).

90. Komukai, T., Yamamoto, T., Sugawa, T. & Miyajima, Y. Upconversion pumped thulium-doped fluoride fiber amplifier and laser operating at 1.47/spl mu/m. *IEEE Journal of Quantum Electronics* **31,** 1880–1889 (1995).

91. Oladeji, A. *et al.* Numerical and experimental investigation of NIR-to-visible energy up-conversion in Er 3+-doped sol–gel SiO 2 powders. *Journal of Materials Chemistry C* **1,** 8075–8085 (2013).

92. Pei, S. & Chun, J. Broadband Solar Spectral Conversion in Near-Infrared Quantum Cutting Ce3+-Tb3+/Yb3+ System for Improving Si Solar-Cell Performance. *IEEE Photonics Journal* **5,** 8400110–8400110 (2013).

93. Federighi, M. & Di Pasquale, F. The effect of pair-induced energy transfer on the performance of silica waveguide amplifiers with high Er/sup 3+//Yb/sup 3+/concentrations. *IEEE Photonics Technology Letters* **7,** 303–305 (1995).

94. Jeon, N. J. *et al.* Solvent engineering for high-performance inorganic–organic hybrid perovskite solar cells. *Nature materials* **13,** 897 (2014).